Università degli Studi di Napoli Federico II
Ph.D. Program in
Information Technology and Electrical Engineering
XXXV Cycle

THESIS FOR THE DEGREE OF DOCTOR OF PHILOSOPHY

Non-Destructive Analysis of Industrial and Biomedical Samples via Advanced TeraHertz Imaging

by

SONIA ZAPPIA

Advisor: Prof. Giuseppe Ruello

Co-advisor: Dr. Lorenzo Crocco

SCUOLA POLITECNICA E DELLE SCIENZE DI BASE
DIPARTIMENTO DI INGEGNERIA ELETTRICA E DELLE TECNOLOGIE DELL'INFORMAZIONE

A mia figlia,
che mi ha insegnato il coraggio
e a non arrendermi mai.

Non-Destructive Analysis of Industrial and Biomedical Samples via Advanced TeraHertz Imaging

Ph.D. Thesis presented
for the fulfillment of the Degree of Doctor of Philosophy
in Information Technology and Electrical Engineering
by

Sonia Zappia

April 2023

Approved as to style and content by

____

Prof. Giuseppe Ruello, Advisor

____

Dr. Lorenzo Crocco, Co-advisor

Università degli Studi di Napoli Federico II

Ph.D. Program in Information Technology and Electrical Engineering

XXXV cycle - Chairman: Prof. Stefano Russo

http://itee.dieti.unina.it

Candidate's declaration

I hereby declare that this thesis submitted to obtain the academic degree of Philosophiæ Doctor (Ph.D.) in Information Technology and Electrical Engineering is my own unaided work, that I have not used other than the sources indicated, and that all direct and indirect sources are acknowledged as references.
Parts of this dissertation have been published in international journals and/or conference articles (see list of the author's publications at the end of the thesis).

Napoli, June 13, 2023

Sonia Zappia

Abstract

Terahertz (THz) imaging is the newest among non-invasive sensing technologies and currently a huge attention is pointed towards its use in several applications. The motivations behind the interest in THz imaging systems can be found in the advantages offered by this technology, including high spatial resolution, use of non-ionizing radiation, and ability to penetrate non-conductive materials like glass, plastic, and cardboard. However, THz potential is still at its early stage and far to be completely assessed and a lot of work remains to be done towards the final industrial implementation and competitiveness of THz technologies.
This thesis aims at the exploration of the potential of THz imaging in the field of food and biomedical industries performing controlled experiments and developing processing techniques to enhance THz capabilities in non destructive inspection (NDI) and material characterization.
Regarding the first research activity, it is known that the detection of foreign body contamination, packaging failures, and items with poor characteristics is a significant concern in the food industry. In this respect, THz systems offer a promising solution due to their non-invasive ability to detect surface defects and foreign bodies contaminations. The thesis aims to perform controlled experiments in order to show the effectiveness of THz technologies in detecting and imaging the presence of contaminants on the surface or a few millimeters deep inside food products. This could open up various possibilities for industrial applications.
The second research activity focuses on the use of THz imaging for the characterization of magnetic scaffolds (MagS), which are used in various biomedical applications. Due to the wide use of MagS in several medical treatments, there is an increasing demand of advanced techniques for their non-destructive quality assessment procedures in order to verify the absence of defects and the distribution of the magnetic nanoparticles (MNPs)

contained in the MagS. In fact, the manufacturing process is often associated with a non uniform final spatial distribution of MNPs loading in the biomaterial, which could compromise the therapeutic efficacy of MagS. This thesis proposes a new approach for MagS characterization using THz imaging, a topic not investigated by the scientific community previously. The proposed approach allows for a quantitative characterization of MagS in terms of their estimated thickness and refractive index. Additionally, it enables to identify the areas of the scaffold wherein MNPs are mainly concentrated and thus, it gives us information about MNPs spatial distribution.

Keywords: THz Imaging, Non-destructive inspection, Food quality, Magnetic Scaffold.

Sintesi in lingua italiana

L'imaging ai Terahertz rappresenta una delle più recenti tecnologie di rilevamento non invasivo ed attualmente è rivolta grande attenzione al suo utilizzo in diverse applicazioni. Le motivazioni alla base dell'uso dei sistemi di imaging ai THz possono essere trovate nei numerosi vantaggi offerti da questa tecnologia, tra cui l'elevata risoluzione spaziale, l'uso di radiazioni non ionizzanti e la capacità di penetrare materiali non conduttivi come vetro, plastica e cartone. Tuttavia, la comunità scientifica è ancora lontana da una valutazione completa delle potenzialità della tecnologia THz e c'è ancora molto lavoro da fare affinché possa essere inserita in un contesto industriale e risultare competitiva rispetto alle tecnologie già esistenti.
Questa tesi ha l'obiettivo di esplorare le potenzialita' dell'imaging ai THz nel campo delle industrie alimentari e biomedicali eseguendo esperimenti controllati e sviluppando tecniche di elaborazione dati per migliorare le capacità dei THz nell'ispezione non distruttiva (NDI) e nella caratterizzazione dei materiali.
Per quanto riguarda la prima attività di ricerca che coinvolge l'industria alimentare, è noto che il rilevamento di contaminazioni da corpi estranei, difetti di imballaggio e di articoli con caratteristiche scadenti rappresenti una preoccupazione significativa per i produttori. A tal proposito, i sistemi ai THz rappresentano una valida alternativa alle tecnologie già esistenti, grazie alla loro capacità di rilevare la presenza di contaminazioni superficiali e di corpi estranei in modo non invasivo. La tesi indaga l'efficacia della tecnologia THz nel rilevare e visualizzare i contaminanti situati sulla superficie o a pochi millimetri di profondità all'interno dei prodotti alimentari, aprendo possibilità per future applicazioni industriali.
La seconda attivita' di ricerca è stata focalizzata sull'utilizzo dell'imaging ai THz per la caratterizzazione di scaffold magnetici (MagS) impiegati in varie applicazioni biomedicali. Il loro ampio utilizzo in diversi trattamenti

terapeutici, ha comportato una richiesta crescente di tecniche avanzate che consentissero di valutarne la qualità attraverso indagini di tipo non invasivo volte a verificare l'assenza di difetti e, più in generale, dedicate alla loro caratterizzazione. Infatti, uno dei problemi che possono presentarsi durante il processo di produzione è che le nanoparticelle magnetiche (MNPs) si distribuiscano in modo non uniforme nella matrice polimerica che li contiene, compromettendo l'efficacia terapeutica dei MagS. In questa tesi viene proposto un nuovo approccio per la caratterizzazione dei MagS utilizzando l'imaging ai THz, il che rappresenta una sfida che non è ancora stata affrontata dalla comunita' scientifica. L'approccio presentato ha permesso di effettuare una caratterizzazione quantitativa dei MagS, in termini di spessore (stimato) e indice di rifrazione. Inoltre, la procedura proposta ha consentito di identificare le aree dello scaffold in cui sono maggiormente concentrate le MNPs e quindi di fornire informazioni sulla loro distribuzione spaziale. Tale argomento non è stato precedentemente oggetto di ricerche scientifiche.

Parole chiave: Imaging ai THz, Indagini Non Invasive, Qualità del cibo, Scaffold Magnetici.

Contents

Abstract ii
Sintesi in lingua italiana iv
Acknowledgements ix
List of Acronyms xii
List of Figures xvii
List of Tables xix
List of Symbols xxi

1 Introduction **1**
1.1 THz Imaging for Food Quality Control 2
1.2 THz Imaging of Magnetic Scaffolds 4
1.3 Scope of the study 6

2 THz systems and Imaging **9**
2.1 THz systems 9
2.1.1 A general overview of the technologies 9
2.1.2 Measurements systems 12
2.2 THz imaging modalities 18
2.2.1 2D Imaging: THz False Color Images 18
2.2.2 3D Imaging: THz tomography 20
2.3 Data processing procedure 24

2.3.1 Noise removal 24
2.3.2 Topographic correction 30

3 THz Non-Destructive Inspection for Food Quality Control 33

3.1 Food Application of THz Imaging 33
3.2 THz inspection of chocolate cream 34
3.2.1 Material: Laboratory Prepared Samples 34
3.2.2 Method: Measurement Protocol 36
3.2.3 Performances of FiCO and TERA THz systems . . . 37
3.2.4 THz imaging results 39
3.3 A further investigation: Packaging Control 49

4 Non-Destructive Characterization of Magnetic Polymeric Scaffolds 51

4.1 Material 52
4.1.1 Magnetic Scaffolds 52
4.1.2 Laboratory Case Studies 52
4.2 Method 53
4.2.1 Measurement Protocol 53
4.3 Characterization of the MagS 55
4.3.1 Thickness Estimation 56
4.3.2 Refractive Index Estimation 58
4.3.3 MNPs Spatial Distribution Estimation 58
4.4 THz results of the Case Studies 60
4.5 Discussion 62

5 Conclusions 69

5.1 Conclusions 69
5.2 Perspectives and future trends 70

Bibliography 73

Author's Publications **83**

Acknowledgements

I would like to express my gratitude to all those who have supported me throughout my academic journey.
First, I extend my sincere appreciation to my esteemed tutors, Prof. Giuseppe Ruello and Dr. Lorenzo Crocco. In particular, I want to express my deep gratitude to Lorenzo for providing me with the opportunity to work in IREA, for constantly challenging me to improve, and for imparting his wisdom and teachings. His guidance has been instrumental in shaping my research.
I am also immensely grateful to Dr. Ilaria Catapano for her steadfast presence by my side, her infinite patience, and her remarkable professionalism. Her guidance, knowledge, and unwavering support have been invaluable to me.
I would like to extend my thanks to Dr. Rosa Scapaticci for her invaluable advice and for always demonstrating kindness and generosity towards me.
I would also like to express my gratitude to the entire doctoral board and our coordinator, Prof. Stefano Russo, for their unwavering support and attentiveness to the needs of us doctoral students. Their dedication to our academic growth has been truly commendable.
I would be remiss if I did not acknowledge the tremendous support of my parents and in-laws. They have been a constant source of love, encouragement, and assistance, especially in taking care of my daughter when I could not. Without their support, I would not have been able to achieve my goals.
To my beloved daughter, I am forever grateful for the joy and light you have brought into my life. Your smiles have brightened even the most challenging moments, and you have been my motivation to persevere.
Lastly, I want to express my deepest appreciation to my partner, Massimiliano, the love of my life. Your unwavering presence, love, and support

throughout this journey have been my rock. Your belief in me and your constant encouragement have fueled my determination to succeed.

The author's work has been carried out in the framework of the PRIN BEST-Food – Broadband Electromagnetic Sensing Technologies for Food quality and security assessment, grant nr B64I19001250001.

List of Acronyms

The following acronyms are used throughout the thesis.

THz	Terahertz
EM	Electromagnetic
MagS	Magnetic Scaffold
MNP	Magnetic Nanoparticles
NDI	Non Destructive Inspection
MD	Metal Detector
XRI	X-ray Imaging
NIR	Near Infrared Imaging
SEM	Scanning Electron Microscopy
TEM	Transmission Electron Microscopy
Micro-CT	Micro Computer Tomography
EOC	Electro Optical Crystal
PCA	Photoconductive Antenna

TDS	Time Domain System
CW	Continuous wave
QCL	Quantum Cascade Laser
BWO	Bake Wave Oscillator
ASOPS	Asynchronous Optical Sampling
BPF	Band Pass Filter
FFT	Fast Fourier Transform
SVD	Singular Value Decomposition
PDM	Propagation Delay Map
MCM	Magnetization Concentration Mask
SuT	Sample under test
I_m	Magnetization Index
I_{md}	Magnetization Distribution Index

List of Figures

1.1 The terahertz region of the spectrum lies between microwaves and infrared, and is characterized by a free-space wavelength between 3 mm to 30 µm. 3

2.1 Typical pulsed THz imaging system. 10

2.2 THz Setup. (a) Reflection mode. (b) Transmission mode. 10

2.3 Zomega Fico system: (a) global view; (b) primary laser source and optical delay line; (c) purge chamber; (d) imaging module. . 13

2.4 Reference signal and noise referred to FiCO system; (a) time-domain waveforms (b) THz power of the spectra in dB scale . . . 15

2.5 TERA System developed by Menlo System; (a) TeraOSE Module; (b) Main Component; (c) Imaging stages, antennas and THz Reflection Head. 16

2.6 Transmission module of TERA System. Tx and Rx indicate emitter and detector; m1-m4 are the mirrors; p is a pin hole in the focal spot used as alignment help. 16

2.7 Reference signal and noise referred to TERA system; (a) time-domain waveforms; (b) FFT Amplitude. 17

2.8 Grayscale False Color THz images bar show different information depending on the adopted processing. The upper image is constructed by peak-to-peak amplitude. The lower image is obtained by plotting the arrival time of the transmitted waveform. (taken from [1]). 20
2.9 Time of flight sensing principle. 21
2.10 THz images reffered to chocolate sample containing metale (a) THz False color; (b) THz radargram. It is possible to distinguish two reflections due to occurrence of different materials. 22
2.11 THz radagrams referred to chocolate cream samples; (a) Raw radargram (Fico system); (b) FFT filtered radargram (Fico system); (c) Raw radargram (TERA system); (d) FFT filtered radargram (TERA system). 26
2.12 Singular Spectrum of A (a) THz FiCo system; (b) THz TERA system. 28
2.13 THz radagrams referred to chocolate cream samples; (a) Raw radargram (Fico system); (b) SVD filtered radargram (Fico system); (c) Raw radargram (TERA system); (d) SVD filtered radargram (TERA system); (e) FFT and SVD filtering (Fico system); (f) FFT and SVD filtering (TERA system) 29
2.14 THz radargrams; **(a)** Noise-filtered data; **(b)** Data after topographic correction. 30

3.1 Chocolate cream samples with surface defects; (a) $S1$: pistachio peel on the surface of the chocolate; (b) $S2$: pistachio partially covered by chocolate. 35
3.2 Chocolate cream samples contaminated by foreign bodies, (a) $S3$: Metal to a depth of 1 mm; (b) $S4$: Sheet of polystyrene to a depth of 1.5 mm 35

3.3 Samples covered by a cap; (a)-(c) samples without cap; (d)-(f) samples as they have been analyzed: $S5$, $S6$, $S7$, respectively. . 36
3.4 Chocolate cream samples contaminated by metal, (a) $S3$: Metal to a depth of 1 mm; (b) Metal to a depth of 3 mm; 37
3.5 THz radargrams referred to cream chocolate samples with metal inside. (a)-(b) metal 1 mm deep inside the cream, data collected with FICO and TERA, respectively; (c)-(d) metal 3 mm deep inside the cream, data collected with FICO and TERA, respectively. 38
3.6 THz false color images referred to the samples $S1$ and $S2$ in fig. 3.1: (a) Maximum amplitude of the signal, $S1$; (b) Maximum amplitude of the signal $S2$. 40
3.7 (a) THz radargram referred to $S1$ (see Fig. 3.1a) - y = 15 mm - The extent of the surface defect ranges from 10 mm to 22 mm; (b) THz radargram referred to $S2$ (see Fig. 3.1b) - y = 20 mm - The extent of the surface defect ranges from 18 mm to 25 mm. . 41
3.8 THz False color images; (a) Maximum amplitude of the filtered signal referred to $S3$, shown in 3.2a; (b) Maximum amplitude of the filtered signal referred to $S4$ in 3.2b. 42
3.9 THz radargrams of the samples $S3$ and $S4$. (a) Metal 1 mm deep inside the chocolate; (b) Polysterene 1.5 mm deep inside the chocolate. 42
3.10 THz images referred to $S5$, shown in Fig. 3.3d (a) THz false color image; (b) THz filtered radargram - y=20 mm (the green dot line in 3.10a); (c) THz waveform - (20,20) mm (marked with the blue x in 3.10a). 43
3.11 THz images referred to $S6$, shown in Fig. 3.3e (a) THz false color image; (b) THz filtered radargram - y=15 mm (the green dot line in 3.11a); (c) THz waveform - (15,15) mm (marked with the blue x in 3.11a). 44

3.12 THz images referred to the sample in 3.3f. (a) THz false color image; (b) THz filtered radargram - y=15 mm (the green dot line in 3.12a); (c) THz waveform - (15,15) mm (marked with the blue x in 3.12a). 45
3.13 Maximum Amplitude of the signal in specific time windows referred to the sample $S5$ in Fig. 3.3d: (a) cap; (b) void between cap and chocolate; (c) chocolate. 46
3.14 Maximum Amplitude of the signal in specific time windows referred to $S6$ in Fig. 3.3e: (a) cap; (b) void between cap and chocolate; (c) chocolate contaminated by plastic. 47
3.15 Maximum Amplitude of the signal in specific time windows referred to the sample $S7$ in Fig. 3.3f: (a) cap; (b) chocolate; (c) metal. 48
3.16 Sugar bags. (a) Photo of a standard packaging; (b) Photo of defect packaging highlighted in the yellow box; (c) THz False color standard packaging; (d) THz False Color defect packaging; (e) THz False color when the sugar has been moved on the left side. 49

4.1 (a) 3D-Insert consisting of a 90°-interlaced fiber architecture, with a fiber diameter of 300 μm, spaced by 300 μm. (b) Image of the 3D structure of the scaffold. 52
4.2 Photos of the samples: (a) scaffold without MNPs named sample 0A; (b)-(d) scaffolds with a different amount of MNPs and referred as sample 1A, 2A and 3A, respectively. 53
4.3 (a) Samples placed on a metal plate. (b) Measurement set up; we will refer to the six configurations with numbers from 1 to 6. 54
4.4 Different fibers orientations used to carry out the measurement. (a) Starting position $\alpha = 0°$. (b) Rotaded by 45°. (c) Rotaded by 90°. 54

4.5 d_1 is the distance between the emitter/receiver and the metal plate. d_2 is the distance between the emitter/receiver and the surface of the scaffold. Δ is the thickness of the object. 56
4.6 (a) Scan Area: external and internal points exploited to derive the averaged A- scans. The yellow circle represents the scaffold. (b) Averaged A Scan from which the value of t_1, highlighted by a red circle, is derived. (c) Averaged A Scan used to derive the value of t_2 and t_3 pointed out by a yellow circle and a green one, respectively. t_4 represents the time that the waveform employs to propagate within the SuT. 57
4.7 Propagation Delay Maps (PDMs). (a) 1A. (b) 2A. (c) 3A. . . . 63
4.8 (a) Photograph of the MagS 1A. (b) MCM 1A. (c) 2D MDM 1A. 64
4.9 (a) Photograph of the MagS 2A. (b) MCM 2A. (c) 2D MDM 2A. 65
4.10 (a) Photograph of the MagS 3A. (b) MCM 3A. (c) 2D MDM 3A. 66

5.1 Maps of permittivity values of unbaked puff pastry. The first map is the reference one, the subsequent ones showing the material's THz behavior when left at room temperature. Data was collected at 30-minute intervals. The maps reveal that certain areas of the pastry gradually dry out over time, resulting in a lower permittivity value. 71

List of Tables

3.1 Scan Area and spatial offset along x and y axes selected for $S1$-$S7$. 37

4.1 Thickness of the MagS, d_m, measured with a manual gauge. . . 55
4.2 t_1, t_2 and t_3 in ps for all the measurement set. 60
4.3 Δ and η values for each measurement and their averages M_{up}, M_{down}, M_{tot} 61
4.4 Thickness of the magnetic scaffolds: d_m is the value measured with a manual gauge - Δ is the averaged thickness estimated for all the measurement set. 61
4.5 t_M, t_{NM} and $T[ps]$ calculated considering the average Δ and the average η for all the six measurement set. 62
4.6 I_m and I_{md} for the MagS. 62

List of Symbols

The following symbols are used within the thesis

Δ	thickness of Mags
η	refractive index
c	Speed of light in a vacuum
I	magnetization index
t	time-of-flight
v	wave propagation

Chapter 1

Introduction

The terahertz (THz) region covers the range of electromagnetic spectrum between 0.1 to 10 THz and lies in the gap between microwaves and infrared as shown in Fig. 1.1. THz waves can penetrate numerous non-metallic materials that may be opaque in the range of visible and infrared light. In fact, one of the most valuable properties of terahertz radiation is its ability to pass through a wide range of substances, thus making it possible to 'see' through many materials such as paper and cardboard, fabrics, plastics, wood, silicon and so on. Moreover, as non-ionizing radiation, THz waves present minimal known health risks [2]. It is essential to also note the existence of chemically specific absorption spectra in the THz range, reflecting molecular transitions and inter-molecular bonds, especially in crystalline organic substances. THz spectroscopy can qualitatively and quantitatively characterize the chemical composition of mixtures containing a wide range of substances [3]. These paired properties penetration and chemical specificity make up the unique feature of THz radiation, not to be found in any other part of the electromagnetic spectrum.
However, the potential and suitability of the THz technology for practical applications such as non-destructive inspections (NDI) and material characterization, have been limited for many years due to the technical difficulty of producing efficient sources and detectors [4]. The origins of THz science and technology, as we know it today, can be traced back to the late 60s and 70s with the study of the response of materials to the excitation of newly developed ultrafast pulsed lasers at time scales in the

range of the picosecond [5]. Such pioneering studies demonstrated the possibility of using semiconductors and electro-optical (EO) crystals such as $LiTaO_3$, $LiNbO_3$, and $ZnTe$ as THz emitters [6, 7]. Research continued in the 80s with improved performance of lasers systems and fabrication of better photoconductive antennas (PCA) for emission and detection of THz waves [8, 9]. The 90s saw the development of better generation and detection techniques based on EO materials [10, 11], the definition of a standard layout for the THz time-domain spectrometer, and the publication of the first papers showing the potential of THz technology as a tool for spectroscopy and imaging [12, 13] applications. Since the late 90s and during the 2000s, THz science has experienced a push from its birthplace in research labs out to commercialization. Among the prominent players involved in the THz technology market, companies, such as Advantest Corp [14], TeraView [15], EMCORE Corp [16], and Terasense Group [17], among others, are focusing on organic as well as inorganic strategies to strengthen their position in the THz technology market.
This evolution, has enabled the introduction of the THz technology to the NDI and material characterization fields, quickly highlighting the advantages of the THz technology for the evaluation and characterization of advanced materials and complex structures.
For these reasons, THz technology are currently exploited in various applications, including medical diagnosis [18], pharmaceutical analysis [19], security enhancement [20], artwork [21], aerospace industry [22] and communication [23].
Despite this significant applications, the transition from laboratory to non-laboratory environments is less certain and smooth as one may wish due to the gap between the capabilities of a technology and specific critical requirements of particular applications.
Within the above described framework, this thesis deals with THz imaging for non-destructive evaluation and in particular with food quality control and characterization of advanced materials for biomedical applications.

1.1 THz Imaging for Food Quality Control

In the food industry, foreign body contamination, packaging failures, or items with poor characteristics (for example, texture and appearance)

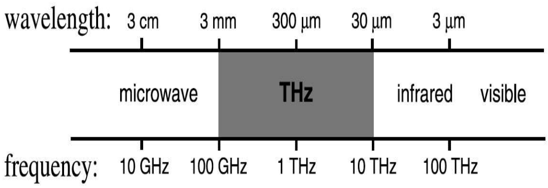

Figure 1.1. The terahertz region of the spectrum lies between microwaves and infrared, and is characterized by a free-space wavelength between 3 mm to 30 µm.

are among the main sources of customers' complaints against manufacturers, resulting in loss of brand loyalty and large recall expenses. To cope with these issues, technologies such as metal detectors (MDs) [24], X-ray imaging (XRI) [25, 26, 27], near-infrared imaging (NIR) [28] and fluorescence imaging [29], have been adopted for monitoring food quality and safety. However, the occurrence of incidents remains significant as each of these technologies have some limitations. For instance, MDs can only detect metallic objects. Whereas, X-rays systems, which are increasingly used in the food production industry for quality control inspection, provide high resolution images but have difficulties in detecting low density objects such as plastic, glass, wood or insects. Furthermore, the use of ionizing radiation is always related to risks involving both operators and the food itself that could be altered. On the other hand, infrared (IR) technologies have the advantage of being fast and safe but they are limited by a poor penetration capability and strong absorption in water. Instead, fluorescence imaging is effective only when objects with fluorescent compounds are investigated. For these reasons, none of these technologies can address all the requirements of the food industry. There is an interest in developing novel technologies that can complement the ones already used along food packaging lines. Among possible candidates, electromagnetic (EM) sensing technologies represent an attractive, cost-effective option. In fact, the most important characteristics of food products that affect their quality (for example, water content and the presence of contaminants) also have a direct influence on their EM properties and can be thus detected by EM devices. However, besides specific technological challenges, when only

a limited portion of the EM spectrum is considered, the overall requirements of agri-food quality control cannot be met. As a matter of fact, at “low” frequencies (e.g., working at microwaves, between few hundreds of MHz and tens of GHz) there are limitations in terms of spatial resolution, whereas higher frequencies (e.g., THz) can detect the presence of contaminants only few mm deep inside the object.
Regarding THz radiations, on which the thesis is focused, recent advancements in the development of compact, cost-effective and effective THz systems motivated a significant interest in exploiting THz waves as a non-destructive and safe inspection tool in several application contexts, among which agro-food industry. THz waves have been successfully used to detect both high-density (aluminum and granite pieces) and low-density (maggots and crickets) foreign bodies in different foods [30]. Moreover, THz spectroscopy combined with chemometric methods has allowed to determine antibiotics and harmful residues, to discriminate genetically modified organisms, and detect adulterations [31]. In addition, reduced-cost THz prototypes capable of fast scanning have been recently proposed from TeraSense and their effectiveness has been shown for dry food inspection [17]. Despite these significant examples, THz potential in food inspection is still at its early stage and far to be completely assessed. For instance, being THz waves strongly attenuated by water, their use for inspecting 'wet' food (like creams) is so far limited and still represents an open issue. In this framework, this thesis aims to perform controlled experiments and to develop processing techniques to enhance THz capabilities in non-destructive inspection of chocolate cream samples. The goal is to detect contaminants whose size is as small as few millimeters, located either above the food surface, underneath the packaging or inside the food.

1.2 THz Imaging of Magnetic Scaffolds

Magnetic polymer-based scaffolds raised a huge interest due to their wide use in several medical applications such as cancer therapy [32], tissue engineering [33] and drug delivery [34]. A magnetic scaffold (MagS) can be obtained by physical loading of magnetic nanoparticles (MNPs) into a polymeric matrix to obtain a multifunctional and theranostic device [35, 36, 37]. However the production process of the MagS is often associ-

ated to a non uniform final spatial distribution of MNPs in the polymeric matrix [38], so that recent and intense progresses on the manufacturing strategies are ongoing. The potential of MagS and the need to control the quality of their productive process motivate the development of procedures for routine and reproducible non destructive characterization of MNP distribution in the polymeric matrix.
Currently, several methods are exploited to analyze MagS such as Micro-Computed Tomography (MicroCTs) [39, 40], Scanning Electron Microscope (SEM) [41, 42, 43], and Transmission Electron Microscopy (TEM) [41, 44, 45] and each one of them has its advantages and drawbacks.

MicroCT uses X-rays to capture the image and, hence, shape and size of the polymer and nanocomposite fibers [39, 40]. The images obtained through the Micro-CT system scan allows for the 3D reconstruction of the nanocomposite fibers and, hence, the distribution of MNPs along the fibers [39]. X-rays system, provide high resolution images but have the disadvantage of using ionizing radiations, always related to risks involving the operator, as well as the material itself that could be damaged [46].

SEM uses a focused beam of high-energy electrons to generate a variety of signals at the surface of solid specimens. The signals derived from electron-sample interactions reveal information about the sample including surface morphology (texture). The shape and the porosity of magnetic scaffolds were observed by SEM images in several works available in literature [41, 42, 43, 47]. However, SEMs are expensive and must be housed in an area free of any possible electric, magnetic or vibration interference. Also, to investigate the sample in depth, slicing and destructive preparation are needed [48].

TEM is a microscopy technique in which a beam of electrons is transmitted through the sample under test to form an image. The image is derived from the interaction of the electrons with the sample as the beam is transmitted through it. TEMs provide topographical, morphological, compositional and crystalline information. The images allow researchers to view samples at a molecular level, making it possible to analyze structure and texture [49]. This type of technique has been used to explore the morphology of the MNPs distributed along the fibers of the scaffolds [41, 44, 45]. However, to obtain a TEM image, samples must be sliced thin enough for electrons to pass through (i.e., usually the specimens has an

ultrathin section less than 100 nm). Therefore, non destructive evaluation is not possible. Moreover, the specimens must be prepared as a thin foil, or etched to be thin enough for the beam to penetrate. Constraints make the sample preparation laborious. Furthermore, other disadvantages are that TEM systems are large and very expensive and their operation and analysis requires special training [48].
Thanks to its unique properties, THz imaging may represent a potential candidate for MagS non destructive characterization. Although, THz technology has been exploited for the detection of damages such as non-impregnated areas in polymer composite materials [50, 2, 51], and for the evaluation of the porosity of the polymeric matrix [52], its application to MagS is a new challenge that has not yet been thoroughly investigated by the scientific community. The proposed approach allows for a quantitative characterization of MagS in terms of their estimated thickness and refractive index. Additionally, it enables to identify the areas of the scaffold wherein MNPs are mainly concentrated and thus, it gives us information about MNPs spatial distribution.

1.3 Scope of the study

The objective of this thesis is to explore the potentials and enhance the capabilities of THz imaging for the NDI and material characterization in the field of food and biomedical industries. The thesis investigates the effectiveness of THz technologies in detecting and imaging contaminants and packaging failures of food products by mean of two THz time domain systems whose results are compared and discussed. The studies carried out allowed the publication of some research products: a chapter of an international book [53], two contributions to international conferences [54, 55] and two contributions to national conferences [56, 57].
Additionally, the thesis proposes a new approach for MagS characterization based on THz imaging, a topic not yet investigated by the scientific community. A quantitative characterization of MagS is provided in terms of their estimated thickness and refractive index. Furthermore, the method presented enables to identify the spatial distribution of the MNPs in the polymeric matrix that contain them. This methodology is designed to be an innovative and practical solution for the biomedical industry, and is pro-

posed as an alternative to existing techniques, offering a non-destructive inspection option. The results obtained allowed the publication of two articles on international journals [58, 59] and two contributions to national conferences [60, 61].
The manuscript is structured as follows.
Chapter 1 introduces the background of this thesis. The basic knowledge of THz radiation and the state-of-art of the development and applications of THz imaging is briefly introduced. Then the discussion is focused on the two-research topic which are the objects of this thesis and the motivations, and the research problems addressed are described.
Chapter 2 provides a brief overview of the main THz technologies and presents the measurement systems, THz FiCO and THz TERA systems, utilized in this work. Then THz imaging modalities are described and the data processing procedures applied to the raw data collected by means of the THz systems are presented.
Chapter 3 is devoted to provide a feasibility study of the potential applications of THz systems in food monitoring control, highlighting their efficacy and potential benefits. In this chapter, several case studies referred to cream chocolate samples are presented and discussed.
Chapter 4 focuses on developing advanced THz imaging techniques for the qualitative characterization of poly(ϵ - capprolactone) (PCL) scaffolds loaded with magnetic nanoparticles that are used in various biomedical applications.
Conclusions and future perspectives follow in chapter 5.

Chapter 2

THz systems and Imaging

2.1 THz systems

2.1.1 A general overview of the technologies

The technology of generating and detecting THz radiation has been constantly evolving in recent decades. A number of approaches have been developed to fill the terahertz gap. Generally, systems for THz imaging can be divided into two main categories based on their operative principle: pulsed and continuous wave systems [62].
Pulsed or time-domain systems (TDS) are based on the generation and detection of an electromagnetic transient (or pulse) that has a duration of few picoseconds. Typical bandwidth ranges from 0.1 to 6 THz for the new generation systems [63]. THz TDS are composed of four principal component: primary source, which is an ultrafast pulsed laser emitting sub 100 fs pulses, THz emitter, THz detector and a time delay stage. There are two main technologies to generate and detect THz pulses: photoconductive antennas (PCAs) and electro-optic crystal (EOC). Usually one emitter and one detector are used, even if technologies based on the use of detectors arrays are available [64]. A schematic of the typical setup for generation/detection of THz pulsed systems is shown in Fig. 2.1. The ultrafast laser beam is split into two parts, one is referred to as the pump beam and the other one is referred to as the probe beam. The pump and probe pulses are derived from the same optical beam and, therefore, have the same pulse duration, which typically has a range between 20 to 120

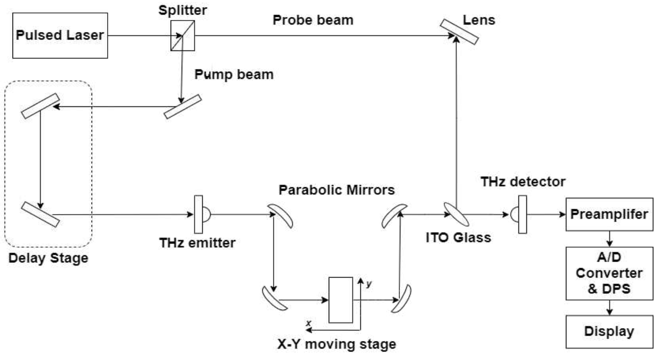

Figure 2.1. Typical pulsed THz imaging system.

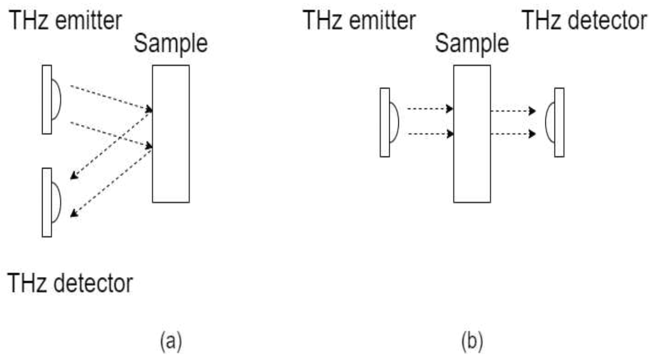

Figure 2.2. THz Setup. (a) Reflection mode. (b) Transmission mode.

fs. The energy of the pump beam is much larger than the energy of the probe beam because the pump beam is used to generate THz pulse. In the most basic configuration, the pump beam generates an electromagnetic transient, through the excitation of a semiconductor or electro-optical material. This electromagnetic transient is the THz pulse. The duration of the THz pulse is in the range of few ps, which is larger than that of the pump beam. The probe beam is used to detect the THz pulse through the inverse process for the THz generation. The detection of the THz pulse provides the waveform, which is the amplitude of the electric field of the THz pulse as a function of the timing difference between probe and pump beams.
The timing difference between pump and probe beams is controlled, thus

the response of the sample to the pump beam as a function of time can be measured very precisely. The most common way to control the timing difference is by using a mechanical delay line in the pump beam. A time delay changes the path length of the beam and, thus, changes the relative timing between the pump and probe pulses. However, more recent technologies have replaced the mechanical delay line with the ASOPS (Asynchronous Optical Sampling) technique which uses a combination of ultrafast lasers and electro-optic modulators to generate a sequence of optical pulses with precisely controlled time delays [65]. By using the principles of optical interference and superposition, these pulses can be combined to create a time-delayed THz waveform without the need for a mechanical delay line. The setup for generation/detection of THz in Fig. 2.1 refers to a THz system working in transmission mode, but the systems can also work in reflection mode as shown in Fig. 2.2 where the two set ups are compared. Continuous wave (CW) systems operate at a single frequency, which depends on the type of THz emitter, and emission is continuous or modulated [62]. The technology behind continuous-wave (CW) THz emitters and sensors involving many different types of technical schemes unlike the methods of broadband THz radiation, mainly relying on ultrafast optical technology. One common way to generate THz emission is by up scaling a fundamental frequency via frequency multiplication. Frequency-multiplied CW systems operate in the lower frequency range of the THz band with maximum frequencies around 0.8 THz (800 GHz). However, systems such as Quantum Cascade Laser (QCL) and Backward-Wave Oscillators (BWO) are capable of emitting at frequencies as high as 5 THz [66, 67]. Another method to generate CW coherent THz radiation is by photo-mixing which is a widely used technique for THz generation due to its simplicity and versatility. In photo-mixing, two lasers with slightly different frequencies are overlapped on a fast semiconductor such as LT-GaAs, which is the photo-mixing media that generates a THz wave with a frequency equal to the difference of the laser frequencies [68]. Changing the laser frequencies will change the difference and, thus, change the frequency of the THz wave. This mechanism allows photo-mixing to sweep a broad range of frequencies. Commonly used CW detectors are thermal ones such as bolometers, Golay cells, and pyroelectric devices [69, 70]. The typical setup for generation/detection of CW THz radiation is conceptually similar to ones discussed in Fig. 2.1

referred to THz TDS; the CW THz radiation is guided in the same manner as for pulse systems, the difference being in the generation of THz radiation, as discussed above.
However, TD and CW THz systems have many differences. TD systems are more complex, expensive and heavy than CW one but they work in a wide band [63]. Moreover, TD systems gather the signal as a function of the time and, thus, allow to reconstruct more information about the investigated samples, provided that appropriate data processing procedures are applied. In addiction, pulsed THz systems allow high temporal resolution, which is crucial for imaging application that necessitate the detection of various layers within a sample. Conversely, CW systems are narrow-band and have a limited tunability but provide high spectral resolution (∼100 MHz). Furthermore, they typically are capable of generating higher output powers ($> 10mW$) than pulsed sources (∼uW). Furthermore, a THz continuous wave system provides a continuous THz signal, which is useful for applications that require a high signal-to-noise ratio, such as the measurement of highly absorbing materials [62]. The continuous THz signal can be integrated over time to provide a stronger signal, making it possible to obtain accurate measurements even in the presence of high levels of noise.
Therefore, both THz pulsed system and CW ones possess their own advantages so the appropriate technologies should be chosen according to the specific requirements of the measurement application.

2.1.2 Measurements systems

THz FiCo System

The FiCO is a fiber coupled Terahertz Time Domain System (TDS) that generates and detects broadband THz pulses, with full waveform sampling rates up to 500 Hz in both transmission and reflection geometries. The system (Fig. 2.3) is made up of three main components: (a) the laser source, (b) the base unit, and (c) fiber optic coupled transmitting and receiving probes reconfigurable in transmission and normal reflection mode. The laser source and the base unit are mounted on a movable optical table, optically connected each other and covered by means of an aluminum

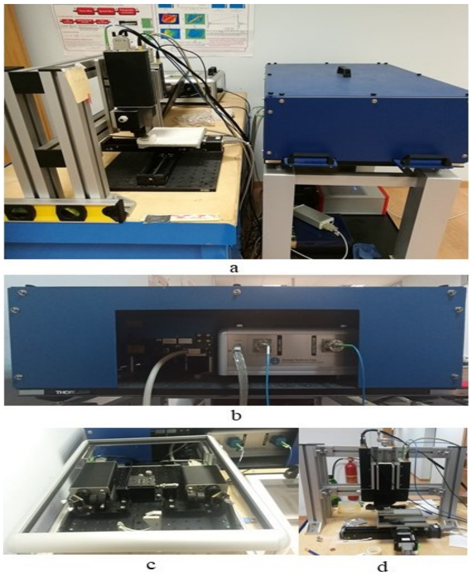

Figure 2.3. Zomega Fico system: (a) global view; (b) primary laser source and optical delay line; (c) purge chamber; (d) imaging module.

box (see Fig. 2.3a-b). The box protects the optical alignment and ensures operator safety with respect to the laser ray. Since the transmitter and receiver are independent and fiber coupled with the base unit, the system can be easily reconfigured to work in transmission and normal reflection measurement configurations.
The FiCO THz-TDS system uses an external free-space or fiber-coupled 1.5 μm pulsed laser with average power $> 200mW$, $< 100fs$, rep rate in the MHz as a pump source that is split into a pump and probe beam used for THz waves generation and detection. A large aperture photoconductive antenna is used to generate THz waves and an electro-optic (EO) crystal is used to detect the THz waves (electro-optic sampling).
The system collects signals into a 100 ps observation time window, which can be moved along a time scan range of 1 ns according to the path length between transmitter and receiver. The waveform acquisition speed can be up to 500 Hz, and the maximum dynamic range (DNR) is 30 dB, while the typical DNR is 20 dB.

The FiCO system is equipped with an ad hoc designed imaging module, which allows an automatic planar scan (see Fig. 2.3d). This module constrains to perform measurements in normal reflection mode. The FiCO system is equipped by an automatic positioning system enabling to scan a 150 mm×150 mm area with physical resolution, i.e., smallest step size, of 120 μm and with a purge chamber, which is suitable to perform spectroscopy while avoiding the effect of water vapor absorption in ambient air. Whatever is the setup, once the object under test has been positioned at a focal distance from the emitter and the receiver, a time-dependent THz waveform is collected and its frequency spectrum is automatically computed. It is worth noting that, when the imaging module is used in reflection mode, at each measurement point, the time-domain-gathered reference signal, i.e., the signal reflected by a mirror, looks like the black waveform shown in Fig. 2.4a, while the gray waveform represents the environment noise measured by turning off the emitter. The frequency spectra of these waveforms are given in Fig. 2.4b. Figure 2.4a shows that the waveform accounting for the mirror reflection is characterized by a main pulse, whose peak arises at 45 ps, and a secondary pulse whose peak is at 90 ps, ariasing from Etalon effect [71]. Accordingly, to avoid replicas affecting the time-of-flight imaging result, an observation time window, which is about 50 ps wide and containing only the main reflected pulse, must be considered. As a consequence, the maximum depth that can be investigated is $d_{max} \leq 50 \cdot 10^{-12} \cdot v/2$. This means that in the most favorable cases ($c \sim v$) d_{max} is about 7 mm. Furthermore, Fig. 2.4b assesses that, despite the nominal spectrum of the gathered waveform is from 0 to 4 THz, the spectrum portion involving frequencies higher than 1.7 THz is too noisy to be considered when reflection measurements are performed.
Moreover, the FiCO system is equipped with a tool which allows to set the scanning parameters (i.e., the step size, the scan area) and provides open access data, which can be visualized and processed after the measurement stage.

THz TERA System

The TERA System [72] developed by MenloSystems is composed of both hardware and software components. In regards to the hardware component, the TERA system, as shown in Figure 2.5, includes the following

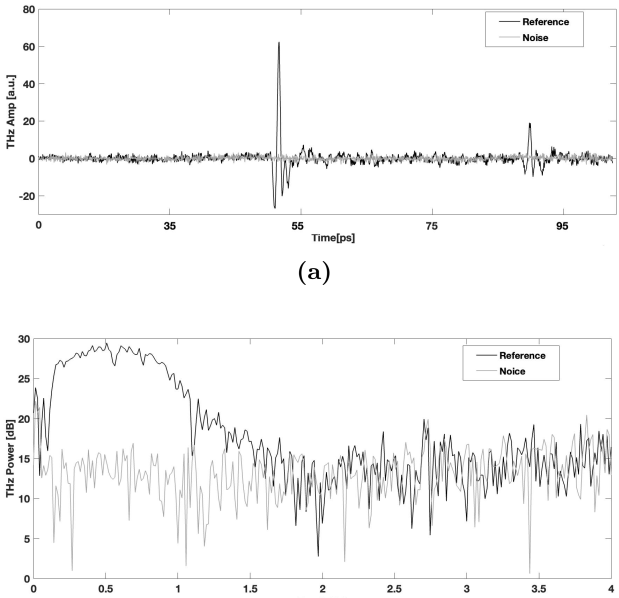

(a)

(b)

Figure 2.4. Reference signal and noise referred to FiCO system; (a) time-domain waveforms (b) THz power of the spectra in dB scale

main components: (a) the TeraOSE module, (b) the imaging stages, and (c) fiber optic coupled transmitting and receiving probes. The TeraOSE module (see Fig. 2.5a) is based on the asynchronous optical sampling technique (ASOPS). This technique allows for high-speed scanning over some nanoseconds of time delay without a mechanical delay line [73], pushing the spectral resolution into the region of hundreds of MHz [74]. TeraOSE, as shown in Figure 2.5a, includes two pulsed femtosecond lasers where one ultrafast laser delivers the pump pulse for the emitter antenna, and the other laser delivers the probe pulse for the detector antenna. TeraOSE lasers operate at a locked repetition rate with a tunable difference, providing the optical pulses for THz emission and detection. The laser pulses are delivered via optical fiber to the THz antenna modules and high-transmission low-loss polymer optics ensure alignment and stability of the THz path. In Fig. 2.5c are shown the fiber-coupled photoconductive antennas which are

(a)

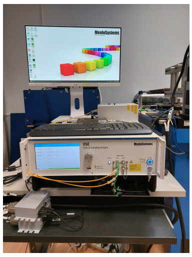

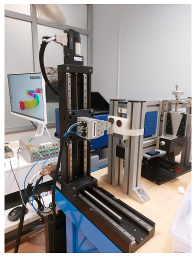

(b) (c)

Figure 2.5. TERA System developed by Menlo System; (a) TeraOSE Module; (b) Main Component; (c) Imaging stages, antennas and THz Reflection Head.

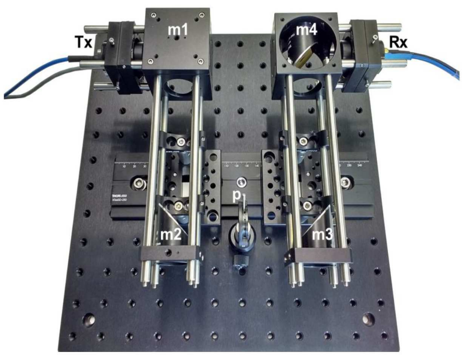

Figure 2.6. Transmission module of TERA System. Tx and Rx indicate emitter and detector; m1-m4 are the mirrors; p is a pin hole in the focal spot used as alignment help.

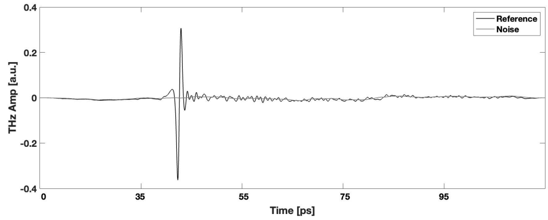

(a)

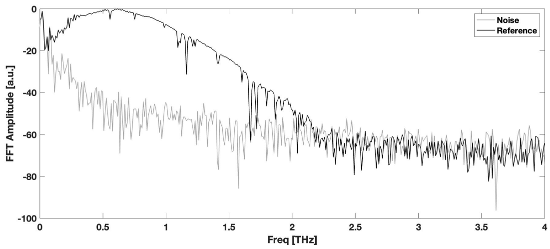

(b)

Figure 2.7. Reference signal and noise referred to TERA system; (a) time-domain waveforms; (b) FFT Amplitude.

inserted in a compact THz reflection head with integrated optics for high-performance measurements. The reflection head and PCA, as depicted in Figure 2.5c, are mounted on imaging stages that are equipped with stepper motors. These motors enable movement along the x-axis and y-axis, resulting in a scan area of 300 mm $\times$ 300 mm and a physical resolution, i.e., smallest step size, of 120 μm. The object under test has been positioned at a specific focal distance from the antennas, which is fixed at approximately 3 mm from the reflection head. The system collects signals into a 100 ps observation time window, which can be moved along a time scan range of 1 ns in the same way as THz FiCO system. Figure 2.7a shows the time-domain-gathered reference signal collected in reflection mode, i.e., the black waveform, and the environment noise measured in the air, i.e., the gray one. The frequency spectra of these waveforms are given in Fig. 2.7b. Herein, the maximum depth that can be investigated for a 100 ps observation time window is $d_{max} \leq 100 \cdot 10^{-12} \cdot \ v/2$. This means that in the most favorable cases ($c \sim v$) d_{max} is about 14 mm. Fig. 2.7b shows

that, despite the nominal spectrum of the gathered waveform is from 0 to 4 THz, the spectrum portion involving frequencies higher than 1.7 THz, is too noisy to be considered, similar to what was observed for the FiCO system.
The system allows spectroscopic measurements by means of the transmission module shown in Fig. 2.6. As for the software component, the TERA system is equipped with a tool which allows to set the scanning parameters (i.e., the step size, the scan area) and the data are saved in text format to ensure easy importing for further data analysis.

2.2 THz imaging modalities

Starting from the beginning of the 21st century, THz imaging has experienced a rapid expansion, and several images methodologies to obtain 2D and 3D characterizations have been developed and tested.
Herein, a particular relevance is given to THz TDS imaging techniques since they have been exploited in this study. Imaging with broadband terahertz (THz) pulses is a powerful technique for non-invasive inspection of a wide range of materials. The unique capability of broadband THz systems to measure the full frequency response of a sample in a single shot enables very accurate identification of sample components and improved depth resolution. Once the broadband THz pulse is generated and detected, as explained in Sec. 2.1, various imaging techniques can be employed. By using different imaging methods and data processing techniques, broadband THz imaging can provide valuable information for various applications, including biomedical imaging, materials characterization, food quality control and cultural heritage [63].

2.2.1 2D Imaging: THz False Color Images

THz imaging is inherently associated with versatile visualization schemes because a THz-TDS image contains much more information than a typical 2-D optical image containing the same number of pixels. Each pixel of a THz-TDS image contains a whole waveform in the time domain, thus the excessive information provides many different display options for a THz-TDS image. Terahertz (THz) imaging can be used to create false color

images in either the time or frequency domains. False color images can be particularly useful for highlighting specific features or materials within an image.
In time domain, several 2D THz false-color images can be obtained by plotting, point by point, different features of the measured wave-forms, such as their amplitude, phase, maximum and minimum value [75]. Consequently, images formed with different features of the data contain different information about the sample. To create a time-domain false color image, the amplitude of the signal (or the time delay between the emitted and detected THz pulses) is first measured for each pixel of the sample under test. This amplitude or time delay is then mapped onto a color scale, with different colors assigned to different values. The resulting false color image provides a visual representation of the object's structure. For instance, Fig 2.8, taken from [1], illustrates this point, showing two THz transmission images of a chocolate bar formed by peak-to-peak amplitude (upper image of Fig. 2.8) and arrival time, i.e., phase of the transmitted THz pulse (lower image of Fig. 2.8). Darker shade indicates lower transmission in the amplitude image and later arrival time in the phase image. Overall, the chocolate is fairly transparent in the THz region. The two images, however, bring out different and nuanced aspects of the sample. First, the amplitude image (upper panel in Fig. 2.8) shows that the almonds in the chocolate bar have higher absorption due to their higher water content, resulting in darker spots. The embossed letters are visible due to scattering at the stepped edges. In contrast, the phase image (lower panel in Fig. 2.8) distinguishes the letters from their surroundings based on their thickness, while there is little contrast between almonds and chocolate because they have similar refractive indices.
It is important to underline that, THz data collected by means of a TD system contains also spectroscopic information. In fact, frequency domain imaging is also possible with the spectrum of the waveform obtained by the Fourier transform [76]. If the sample contains a material having spectral fingerprints, the material's characteristics can be brought out in the image by considering amplitude or phase at the specific frequencies of the spectral fingerprints [76].

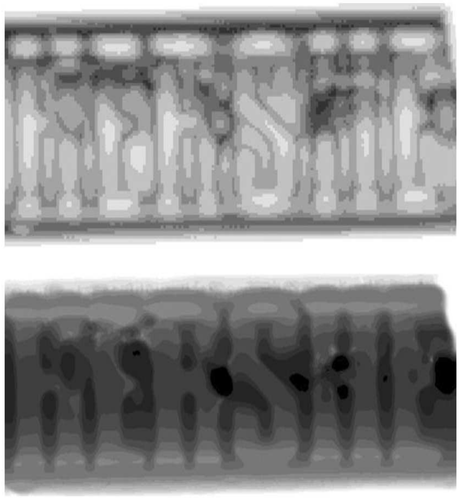

Figure 2.8. Grayscale False Color THz images bar show different information depending on the adopted processing. The upper image is constructed by peak-to-peak amplitude. The lower image is obtained by plotting the arrival time of the transmitted waveform. (taken from [1]).

2.2.2 3D Imaging: THz tomography

Tomography refers to the cross-sectional imaging of an object by measuring either the transmitted or reflected THz signal [77]. Several tomography techniques have been developed exploiting the high transparency of non-polar, non-metallic materials in the THz range.

THz Time of Flight Imaging

THz time-of-flight imaging (TOF) also known as THz pulsed imaging (TPI) has the unique property of providing a 3D "map" of the object by exploiting data collected in reflection mode [78]. The broad bandwidth of the THz radiation is an additional advantage in a reflection mode, since it permits one to obtain depth information and therefore construct a full three-dimensional representation of an object [1]. This technique was used for the first time by Mittleman and coworkers to produce the internal structure of a 3.5 inch floppy disk [13]. In brief, when the object is probed

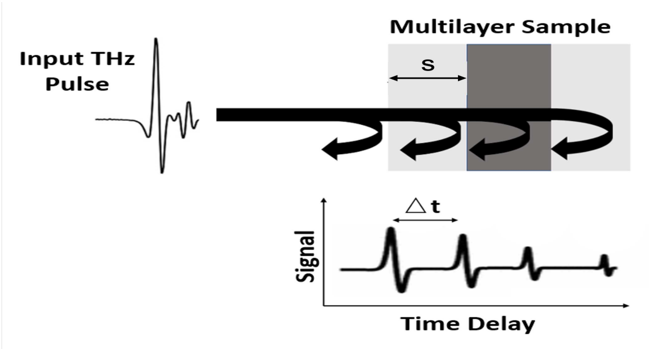

Figure 2.9. Time of flight sensing principle.

by a pulse signal, the reflected waveform is collect as a function of the time and the contribute due to the interaction between different materials appears as pulses at different time delays. Therefore, time-of-flight analysis of the waveforms can map out the internal layer structure (if the object is non-metallic). In particular, the amplitude of each pulse in the train provides information about the magnitude of the dielectric change across the interface from which it originated [1]. The time delay between successive pulses in the train provides information about the inner stratigraphy. In fact, performing this kind of measurements on samples with smooth parallel transparent layers, it is possible to obtain the spatial variation of the refractive-index profile along the direction of propagation of the THz beam [1].

Figure 2.10 shows a pair of images collected using this reflection geometry, referred to a cream chocolate sample containing metal. The image in Fig. 2.10a shows a THz false color image, displaying the maximum amplitude of the reflected THz field as a function of the position of the object. In this image, it is possible to distinguish the metal as it reflects essentially all of the THz radiation, differently from the chocolate. Figure 2.10b shows a single line scan along y = 11 mm in the THz false color image (see the dot line in Fig. 2.10a) where it is possible to distinguish two reflections due to occurrence of different materials (i.e., air-chocolate interface, chocolate-metal interface). Such image, referring as THz radargram, is a two-dimensional image, wherein the horizontal axis is the space axis and represents the measurement line, while the vertical axis is the

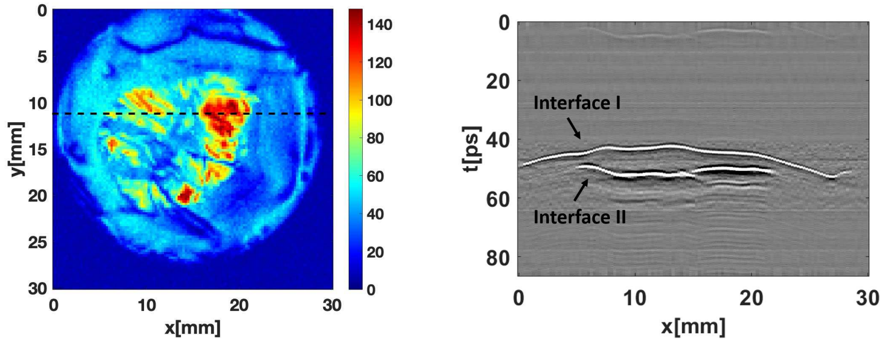

(a) (b)

Figure 2.10. THz images reffered to chocolate sample containing metale (a) THz False color; (b) THz radargram. It is possible to distinguish two reflections due to occurrence of different materials.

time axis and represents the time of flight, that is, the time t that the waveform employs to propagate from the emitter to an electromagnetic discontinuity and to go back to the receiver (see Fig. 2.9, where the ToF sensing principle is sketched). The time of flight t is related to the distance d between THz probes and detected discontinuities by:

$$t = \frac{2d}{v} \tag{2.1}$$

v being the electromagnetic wave propagation velocity into the object. Therefore, a THz radargram provides a cross-sectional representation of the inner features of the object, which gives information about position and thickness of possibly inner layers. A 3D characterization is obtained by collecting radargrams along parallel profiles and visualizing all together the stored data.

In addiction, in cases where the object under test is made of various materials situated at different depths, THz TOF imaging allows to plot the signal amplitude occurring in a specific time window. This creates depth slice images, which allow the visualization of the layers or inclusions present within the object. An example of this application is reported in [21] where the different layer of an ancient mortar specimen is visualized.

THz TOF imaging is effective because different materials exhibit different behavior when illuminated by THz radiation. In principle, the spatial distribution of the refractive index can be retrieved. On the other hand, it is important to take into account that the reflectivity of an object depends not only on its refractive index, but also on the surface roughness, polarization of incident THz radiation and more geometric factors [20].

THz diffraction Tomography

THz diffraction tomography aims at reconstructing the refractive index of the investigated object by exploiting the relation existing among diffracted THz waves and electromagnetic parameters of materials. This relationship is described by Maxwell's equations and depends on the relative position of the object with respect to THz transmitting and receiving probes. More precisely, diffraction tomography exploits a linearized model to describe the interaction between THz wave and material, which is obtained by introducing approximations commonly exploited in electromagnetic sensing, like Born or Rytov approximations. Hence, the imaging is performed by applying the Fourier diffraction theorem [79].
The first implementation of THz diffraction tomography was reported in [80], wherein an imaging approach based on the Born approximation was proposed and exploited to characterize a polyethylene cylinder. Despite its potentialities, THz diffraction tomography has a limited applicability due to the complexity of the required measurement setup, which must allow acquisition of 2D images of the diffracted THz field over a wide range of angles. This unconventional approach involves also a time-consuming data acquisition step, which is not suitable for many applicative scenarios. Another limitation is the power of the probing signal, which constrains the investigation depth significantly, due to material attenuation. Indeed, the very low SNR hinders the imaging, and poor reconstruction capabilities are experienced.

THz Tomosynthesis

Tomosynthesis allows reconstruction of few slices of the investigated object without requiring measurement in all directions. Tomographic images are obtained, indeed, by moving THz emitter along a linear trajectory in such a way to cover a limited angle of view, which range from -50 to 50 degrees usually. Then, THz waveforms transmitted through the object are measured on a detector plane opposed to the emitter plane. Accordingly, for each point of view, a radiography of the object is obtained, similarly to the standard tomography, and the imaging approaches developed for the standard tomography can be exploited. Tomosynthesis is often used for medical imaging [81] and can be considered a tomography with a reduced amount of data. This implies a restriction on the imaging performance that can be in principle achieved but allows a not trivial simplification of the measurement setup

2.3 Data processing procedure

The raw data collected by the THz systems are processed by means of different strategies aiming at improving the quality of the images obtained. This is necessary to mitigate the effects of environmental noise, which are unavoidable in the measurement process. These procedures improve the signal-to-noise ratio, which is particularly important in THz imaging due to the potential impact of ambient water vapor on the measured waveform. This section aims to describe the data processing procedures employed to enhance the quality of the raw data collected by the systems described in Sec. 2.1.2 operating in reflection mode.

2.3.1 Noise removal

Fourier Filtering

Band-pass filters are often used in THz imaging systems to selectively pass the desired frequency range of THz radiation while rejecting unwanted frequencies outside of that range. This can help to improve the signal-to-noise ratio and increase the contrast of the produced images. The filter can help to remove unwanted frequencies that may be present in the THz radiation, such as noise or interference from other sources, and improve the quality of the resulting images. Herein, the aim is to remove the undesired low and high frequency signal components by focusing on data collected in reflection mode. This is performed by selecting the range 40 GHz - 1.7 THz. This choice is due to the fact that, as discussed in 2.1.2,

the frequency spectra of the waveforms gathered with the adopted THz devices (Figs. 2.4b and 2.7b) present a low frequency noise at about [5 GHz- 30 GHz] introduced by the measurement system, and for frequency higher than 1.7 THz the collected data present a noise whose amplitude may be comparable with the useful signal.
In this framework, the raw data is processed according to the procedure described in the following. First, the direct fast Fourier transform (FFT) is used to obtain the spectra of all the time-dependent THz waveforms. Then, the effective frequency range of the data is fixed as discussed above and the band from 40 GHz to 1.7 THz is selected. Finally, the chosen portion of the spectrum of each THz signal is transformed in time domain by means of the inverse FFT (IFFT).
Therefore, let s(t) the raw measured THz signal at a certain position of the transmitter and receiver, the filtered signal is given by :

$$\hat{s(t)} = IFFT(\Pi(FFT(s(t)))) \tag{2.2}$$

wherein Π denotes the band pass filter used that is a pass-band rectangular filter with a central wavelength equal to 0.83 THz. It is worth observing that the restriction of the spectra at the effective frequency range of the signal affects the range resolution, that is, the depth resolution when a normal incidence is assumed for the probing signal. According to the diffraction theory [82], the range resolution is:

$$\Delta R = \frac{v}{2B} \tag{2.3}$$

where v is the wave propagation velocity in the probed medium and B is the considered bandwidth. To point out the effect produced by the described procedure, two raw radargrams (referred to the THz imaging systems described in sec. 2.1.2) and the corresponding filtered ones are shown in Fig. 2.11. By observing the filtered radargrams (see Figs. 2.11b and 2.11d), it can be noticed that the band-pass filter improves the quality of both raw radargrams.

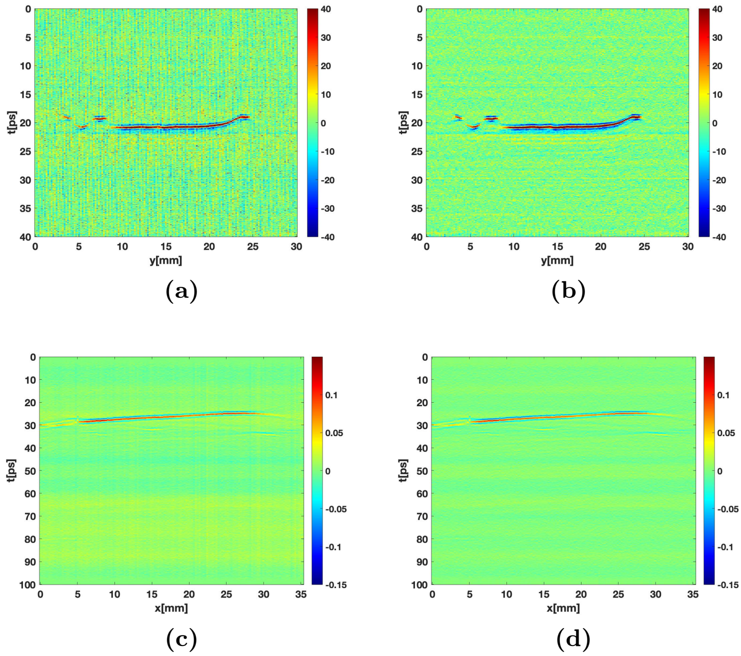

Figure 2.11. THz radagrams referred to chocolate cream samples; (a) Raw radargram (Fico system); (b) FFT filtered radargram (Fico system); (c) Raw radargram (TERA system); (d) FFT filtered radargram (TERA system).

Singular Values Decomposition

Singular Value Decomposition (SVD) is a powerful mathematical tool that can be used to analyze and filter signals. It is a method for decomposing a matrix into its constituent parts, which can be used to reveal important information about the signal [83]. In the context of signal filtering, SVD can be used to identify and remove noise from a signal. By decomposing the signal matrix into its singular values and vectors, it is possible to identify the dominant components of the signal, which are often the parts of the signal that contain the most information. These dominant components can be used to reconstruct the original signal, while the noise components can be removed or reduced in amplitude.
From a mathematical point of view, the SVD can be briefly described as

follows. Let A denote an NxM matrix, whose rows and columns represent the N measurement points and the time samples M discretizing the observation time window, respectively. The singular value decomposition of the matrix, according to the theory, is :

$$A = USV^T = \sum_{i=1}^{Q} \sigma_i \mu_i v_i^t \tag{2.4}$$

where the matrix U is a NxN matrix whose columns are the n orthonormalized eigenvectors associated with the n largest eigenvalues of AA^T, and represent the left singular vectors of A. The matrix V is a MxM matrix whose columns are the orthonormalized eigenvectors of A^TA [84] and represent the right singular vectors of A. S is the NxM diagonal matrix whose elements are the singular values of A arranged in a decreasing order of magnitude and Q $\leq min\{M, N\}$ is the rank of A [79]. A can be regarded as a 2D or 3D image, so according to SVD theory [85], may be decomposed into a sum of rank one matrices (base images) given by $\mu_i \cdot v_i^t$ for i=1,. . . .Q. The singular value σ_i denotes the contribution of the ith base image to the data matrix A. Therefore, the decreasing order of σ_i implies that the contribution in Eq. 2.4 given by the ith base image decreases as i approaches Q. Accordingly, it is reasonable to assume that the first P base images represent the significant part of the data matrix, while the other Q-P base images mainly account for the noise on data. Based on the above considerations, noise may be filtered out, while preserving the image details, by truncating the summation in Eq. 2.4 at the threshold P<Q, i.e., the noise-filtered data matrix $\tilde{\mathrm{A}}$ is obtained by truncating the SVD at the threshold P.

$$\hat{A} = \sum_{n=1}^{P} \sigma_i \mu_i v_i^t \tag{2.5}$$

A suitable value of P has to be determined and this, theoretically, depends on the specific data matrix. Usually a good choice is to set P in such a way that the energy of the filtered data matrix is about the 90–95% of the energy of the collected matrix. On the other hand, in the case of THz imaging, this pratical rule is replaced by a most convenient criterion, which accounts for the characteristic decreasing behavior of the singular values. In fact, it is observed that the singular spectrum of a generic data matrix

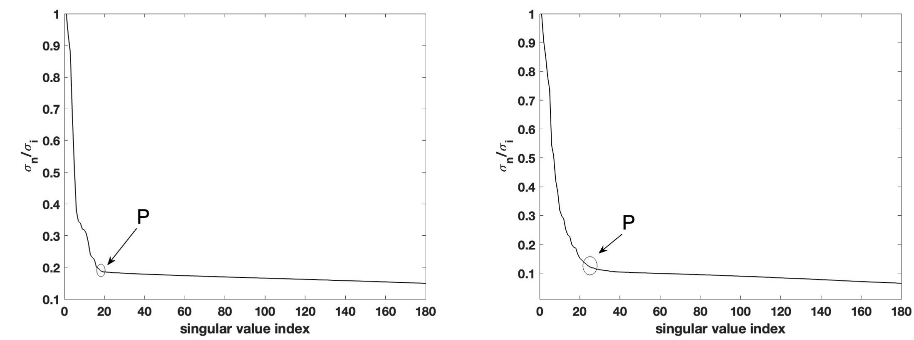

(a) **(b)**

Figure 2.12. Singular Spectrum of A (a) THz FiCo system; (b) THz TERA system.

is characterized by a fast decay followed by a smooth (almost constant) behavior of the singular values [21]. Accordingly, a most suitable rule is to choose P as the index of the singular value in correspondence of the point where the spectrum changes its slope. In other words, P is fixed as the index of the singular value where the fast decay of the singular values is followed by the smooth one (see Fig. 2.12). This index is referred to as knee point.

Figures 2.13(a-d) show the raw data collected by both THz systems described in sec. 2.1.2, processed by means of Singular Value Decomposition (SVD) filtering procedure. It is evident by comparing figs. 2.13a and 2.13c and figs. 2.13b and 2.13d that the quality of the image has been enhanced compared to the original raw data. However, there is still a noticeable presence of background noise in the form of yellow lines as shown in the figures 2.13b and 2.13d. Figure 2.13e-f shows the results obtain when the SVD filtering procedure is applied to the FFT filtered data and demonstrates an improvement of the image quality. It is worth noting that the SVD filtering technique enables the elimination of noise components without compromising the image resolution.

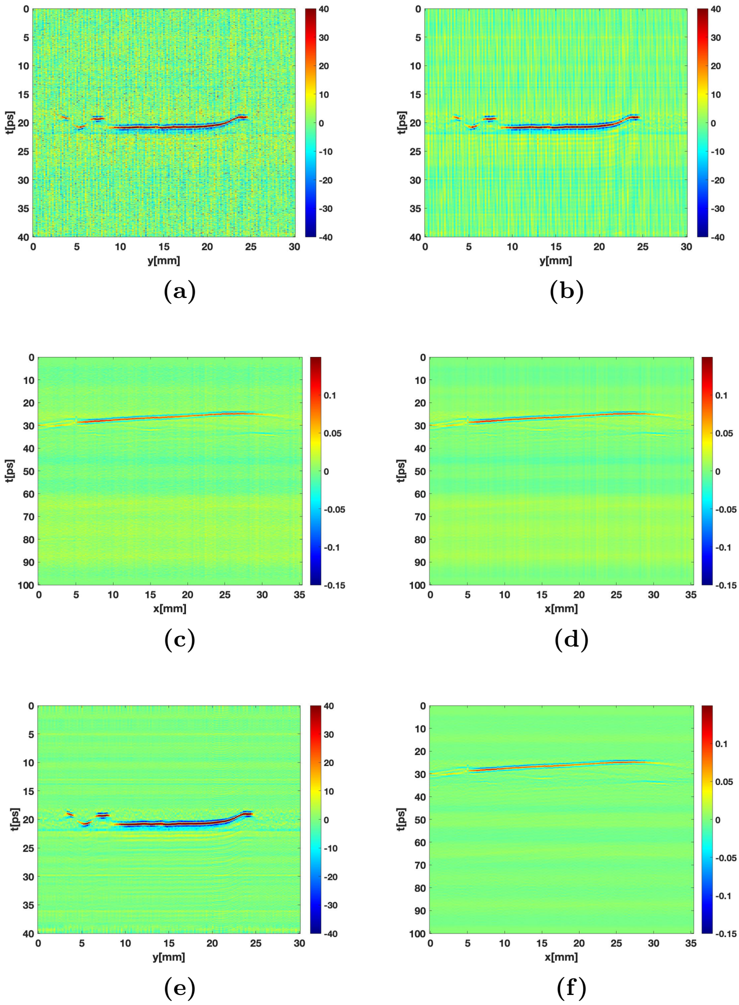

Figure 2.13. THz radagrams referred to chocolate cream samples; (a) Raw radargram (Fico system); (b) SVD filtered radargram (Fico system); (c) Raw radargram (TERA system); (d) SVD filtered radargram (TERA system); (e) FFT and SVD filtering (Fico system); (f) FFT and SVD filtering (TERA system)

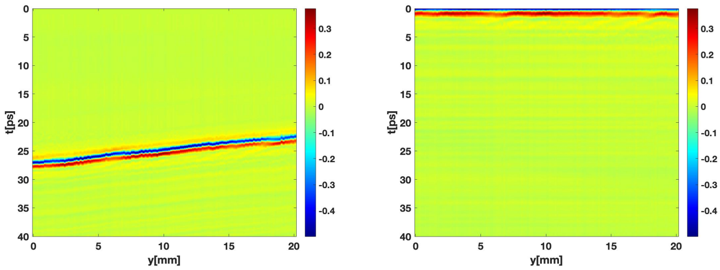

(a) **(b)**

Figure 2.14. THz radargrams; **(a)** Noise-filtered data; **(b)** Data after topographic correction.

2.3.2 Topographic correction

The sensitivity of THz waves to the surface topography of the surveyed object may affect significantly the ability to properly image the object surface and its inner structures. To overcome such a problem, a topography correction procedure is adopted. This strategy aims at correcting the surface topography of the sample by aligning the pulses due to the air-sample interface. This method allows to clearly see and identify the different layers in the sample if these are parallel one to each other and parallel to the air-sample interface. The topography correction is applied in different ways, taking into account the structure of the sample and the objectives of the analyses to be carried out. The adopted procedure performs an alignment of the first reflection by setting the time zero, i.e., t = 0 ps or, correspondingly, the depth z = 0 mm, if the air-sample interface provides the maximum reflected pulse, the alignment is easily performed by looking for the maximum value of the recorded signal. Figures 2.14a and 2.14b show the THz radargrams obtained before and after the application of the topography correction procedure to the noise-filtered radargram.

As previously stated, this procedure is effective when the first interface causes the maximum peak. However, sometimes the hidden layers of the material may have a higher reflectivity than the surface layer, such as when there are metallic materials in the object under test. In these cases, the first interface no longer represents the maximum peak and the alignment is performed by finding the maximum of the recorded signal between the beginning of the measurement window (t_0) and the time position at which the air-sample interface response occurs (t_1).

Chapter 3

THz Non-Destructive Inspection for Food Quality Control

This chapter contributes to the assessment of THz imaging potentialities in food quality controls. The study is carried out by investigating laboratory-prepared food samples by means of two TD THz systems in order to understand how the achievable performances depend on the adopted THz systems. The attention is mainly focused on chocolate cream samples, which have been contaminated or not by surface and shallow subsurface foreign bodies, and are surveyed with and without a cover mimicking and packaging. The results demonstrate the capability of THz waves to image surface defects and to locate foreign bodies that affect product quality in packaged food products.

3.1 Food Application of THz Imaging

THz imaging has several potential applications in the food sector due to its ability to penetrate non-conductive materials and provide high-resolution images. It is worth pointing out that, non-polar and non-metallic materials such as plastic, cardboard, wood and other common packaging materials are transparent to THz radiation and have only a very weak interaction with THz waves. This makes THz imaging an attractive

tool for the inspection of packaged products. The use of THz waves allows, on the one hand, to detect unwanted objects that compromise the safety of the product and, on the other hand, to check defects of the sample under test by controlling its integrity. In this way, defects such as irregular shapes, breaks and even the absence of the product itself in the packaging can be detected to ensure quality. On the other hand, it is worth noting that THz waves are strongly attenuated by water, so it is possible to detect impurities present only a few mm deep inside the product, especially if we consider wet foods. Despite the presence of various examples in literature [63, 86], the study of THz potential in food inspection is still at an early stage and far to be completely assessed.
As a contribution to this topic, experimental research activities have been carried out with the main interest towards the study of potentialities and limits offered by THz imaging in the investigation of chocolate cream. Further experiments have regarded the imaging capabilities of packaging defects.

3.2 THz inspection of chocolate cream

3.2.1 Material: Laboratory Prepared Samples

The analyses are carried out on 7 laboratory-prepared samples that are made by 7 mm high plastic support filled with a chocolate cream.
The samples are divided into three categories: 1) samples with surface defects; 2) samples containing foreign bodies inside them; 3) samples covered by a cap mimicking commercial packaging, with and without defects. Fig. 3.1 shows two samples of the first category (i.e., samples with surface defect), named $S1$ and $S2$. In the first case there is a surface defect consisting of a piece of pistachio peel (see Fig. 3.1a), while in the second case a piece of pistachio shell, mimicking the defect, is partially covered by chocolate cream as shown in Fig. 3.1b.
Fig. 3.2 shows two samples of the second category (i.e., uncovered samples with foreign bodies), which are referred to $S3$ and $S4$. In the first case metal has been hidden 1 mm deep inside the chocolate cream, mimicking the contaminant (see Fig. 3.2a) and in the second case a sheet of polystyrene contaminated the sample to a depth of 1.5 mm (in Fig. 3.2b).

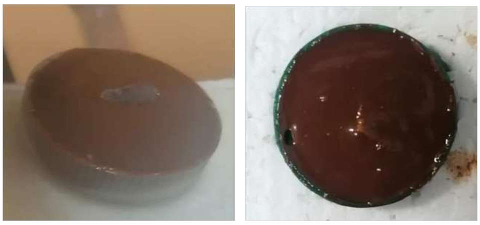

(a) (b)

Figure 3.1. Chocolate cream samples with surface defects; (a) $S1$: pistachio peel on the surface of the chocolate; (b) $S2$: pistachio partially covered by chocolate.

(a) (b)

Figure 3.2. Chocolate cream samples contaminated by foreign bodies, (a) $S3$: Metal to a depth of 1 mm; (b) $S4$: Sheet of polystyrene to a depth of 1.5 mm

Finally, Fig. 3.3 show three covered samples of the third category (i.e., samples covered by a cap mimicking a commercial packaging). Specifically, Figs. 3.3a-3.3c show the sample without cap, while Figs. 3.3d-3.3f show the same samples as they have been analyzed, i.e. covered by a non-metallic package. The samples are named $S5$, $S6$, $S7$, respectively. The packages in Figs. 3.3d and 3.3e are formed by a double layer (i.e., plastic and paper), the one in Fig. 3.3f is made by a single paper layer. The sample in Fig. 3.3a, mimics the standard case, i.e the chocolate without defect; the sample in 3.3b accounts for the presence of a contaminant, which is 13 mm $\times$ 13 mm plastic fragment, located on the chocolate surface; the third sample in Fig. 3.3c represents the case of a 20 mm $\times$ 20 mm metal

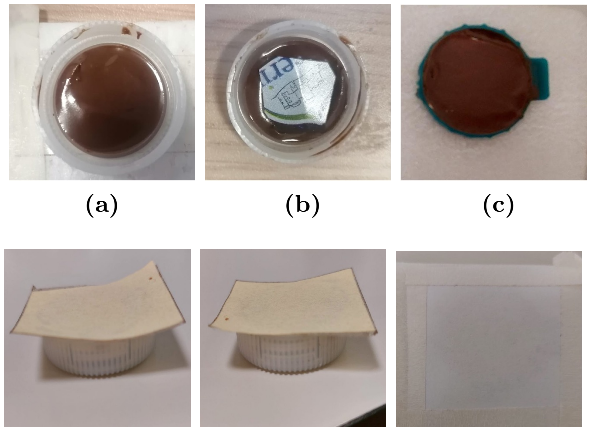

(a) (b) (c)

(d) (e) (f)

Figure 3.3. Samples covered by a cap; (a)-(c) samples without cap; (d)-(f) samples as they have been analyzed: $S5$, $S6$, $S7$, respectively.

fragment hidden at a depth of about 1 mm into the chocolate cream.

3.2.2 Method: Measurement Protocol

The procedure used to carry out the measurement of the samples $S1$-$S7$ can be summarized in the following steps.

1. The object under test is placed at the focal distance from THz emitters;

2. The scanning area is set and the spatial offset along x and y axes is selected in agreement with the spatial variability of the geometrical features of the investigated samples (see Tab. 3.1);

3. The raw data are processed as described in Chapter 2.

THz measurements are performed in reflection mode and in uncontrolled environment conditions with temperature values in the range 28°C - 30°C and humidity percentages from 30% to 35%.
Table 3.1 contains the scan area and the spatial offset along x and y axes selected for the samples analyzed.

Table 3.1. Scan Area and spatial offset along x and y axes selected for $S1$-$S7$.

Samples	Scan Area [mm × mm]	Spatial offset [mm]
$S1$	35 × 35	0.25
$S2$	40 × 40	0.25
$S3$	30 × 30	0.25
$S4$	35 × 35	0.25
$S5$	40 × 35	0.25
$S6$	40 × 40	0.25
$S7$	40 × 35	0.25

(a) (b)

Figure 3.4. Chocolate cream samples contaminated by metal, (a) $S3$: Metal to a depth of 1 mm; (b) Metal to a depth of 3 mm;

3.2.3 Performances of FiCO and TERA THz systems

The measurements are carried out by means of the FiCO and TERA THz systems, which are both described in Chapter 2. In the preliminary phase, it was deemed appropriate to analyze the same samples with both systems to compare their results. The objective was to verify the consistency of the results obtained with the two systems, to ensure that the measurement system used to inspect the sample did not affect the results. To this end, two additional laboratory samples of chocolate cream were used (see Fig. 3.4); the first containing metal at a depth of 1 mm (Fig.

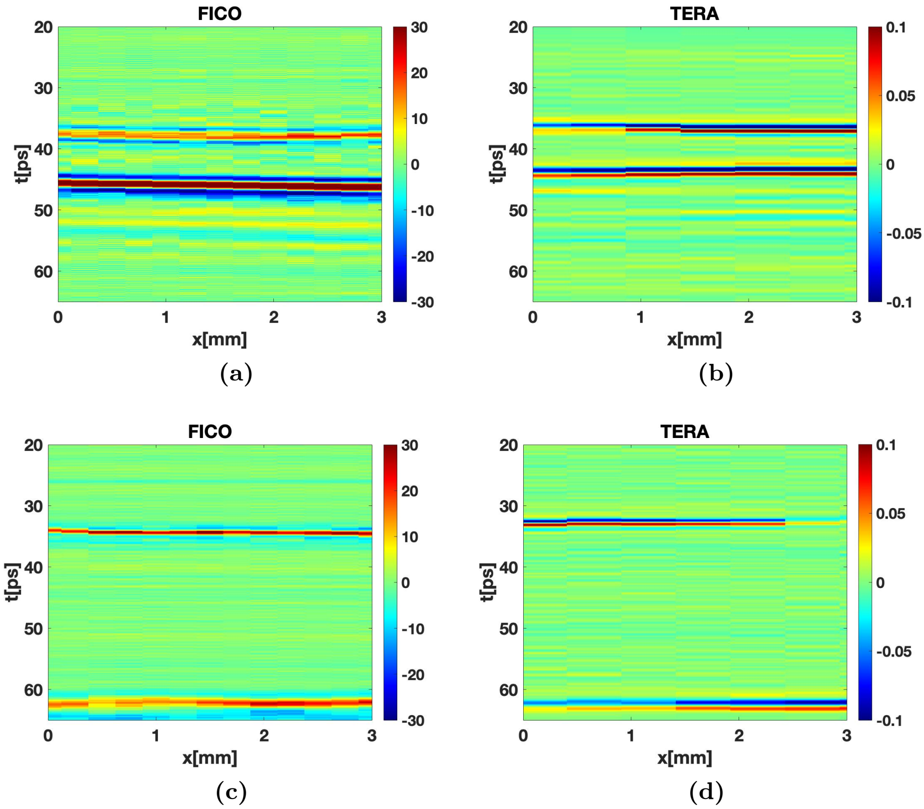

Figure 3.5. THz radargrams referred to cream chocolate samples with metal inside. (a)-(b) metal 1 mm deep inside the cream, data collected with FICO and TERA, respectively; (c)-(d) metal 3 mm deep inside the cream, data collected with FICO and TERA, respectively.

3.4a), and the second at a depth of 3 mm (Fig. 3.4b). Only a few scan lines were collected along the y-axis of these samples, with a spatial offset along x of 0.5 mm, as large amounts of data were not necessary to verify the consistency of the results. Fig. 3.5 shows the THz radargrams referred to a central y measurement line of the chocolate samples. Specifically, comparing Fig. 3.5a and Fig. 3.5b (corresponding to the sample containing metal at a depth of 1 mm), it can be observed that the first

reflection due to the air-sample interface, and the second one due to the sample-metal interface, are delayed in both cases by approximately 8 ps. In fact, Fig.3.5a and Fig. 3.5b (i.e., corresponding to data collected with the FiCO and TERA systems, respectively) show a first reflection of the sample at approximately t=36 ps and a second reflection due to the metal at t=44 ps.
A similar behavior can be observed in the THz radargrams in Figs. 3.5c and 3.5d, which refer to the case where the metal was placed at a depth of approximately 3 mm in the chocolate cream. In this case, the time delay between the two reflections is approximately 30 ps; Figs. 3.5c and 3.5d show the first reflection due to the air-sample interface at about 33 ps, and the second reflection due to the metal inclusion appearing at approximately 63 ps. The only difference that can be observed by looking at the colorbars of the radargrams in Fig. 3.5 is related to the amplitude of the measured signals; in fact, the FiCO system shows higher intensity values compared to those measured with the TERA system, because the FiCO system delivers higher power. Therefore, it is possible to conclude that, except for a scaling factor in amplitude, the coherence of the measurements is demonstrated, as expected considered the similar nature of the two systems used (i.e., both are TD systems). From this point on, the results will be shown without specifying the measuring system used to perform the analysis, as it has been shown that the instrumentation does not affect the obtained results.

3.2.4 THz imaging results

The results referred to the cream chocolate samples introduced in Sec. 3.2.1, shown in Figs. 3.1-3.2-3.3, are presented in this section. The results are obtained using the time-of-flight imaging technique described in Chapter 2. For the sake of brevity and to avoid repetition, imaging results referring to only one of the two considered systems are reported in the following.

Surface defects detection

THz false color images of the samples $S1$ and $S2$ in Fig. 3.6, show the maximum values, point by point, of the filtered data. Specifically,

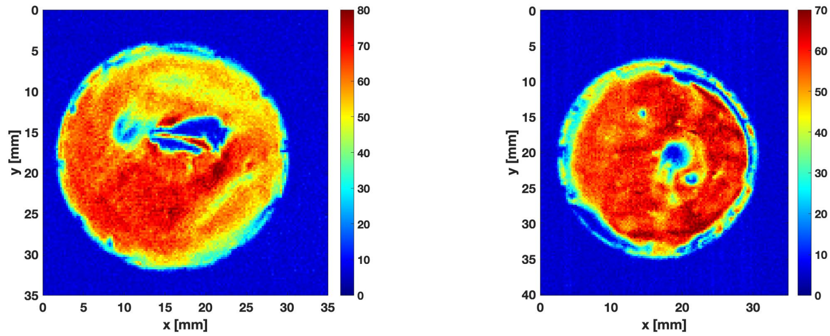

(a) (b)

Figure 3.6. THz false color images referred to the samples $S1$ and $S2$ in fig. 3.1: (a) Maximum amplitude of the signal, $S1$; (b) Maximum amplitude of the signal $S2$.

Fig. 3.6a demonstrates THz imaging ability to accurately represent the pistachio peel on the surface of the chocolate cream (see 3.1a) and Fig. 3.6b to detect the pistachio shell partially hidden inside the chocolate cream sample (see Fig. 3.1b).

As further proof of the ability of THz imaging techniques to effectively identify the presence of surface defects, THz radargrams of the filtered data, are shown in 3.7. Fig. 3.7 shows THz radargrams, referred to the samples $S1$ and $S2$, for y= 15 mm and for y= 20 mm, respectively, that corresponds to areas where the contaminants are present. By observing Fig. 3.7a, it is possible to note the presence of the surface defect ranging from 10 mm to 22 mm.

Fig. 3.7b shows that the chocolate's response changes following the shape of the partially hidden surface contaminant. It is worth pointing out that, as shown in Fig. 3.1b, the pistachio shell only partially emerges from the chocolate cream and it is not possible to distinguish its shape. Notably, the THz radargram in Fig. 3.7b allows to evaluate the extent of the defect ranges from 18 mm to 25 mm.

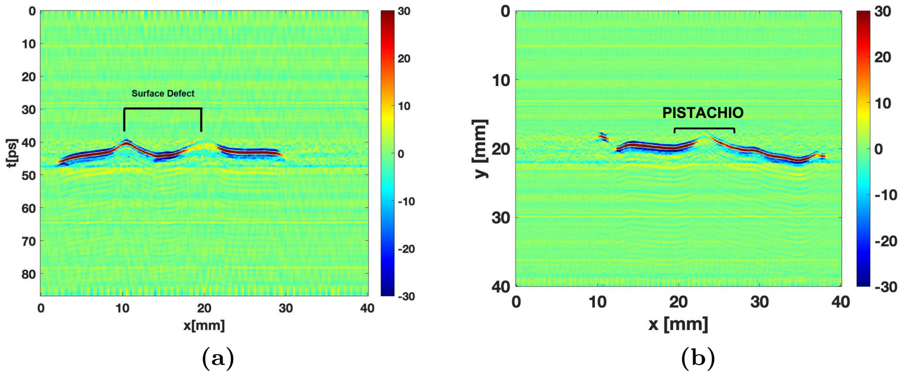

Figure 3.7. (a) THz radargram referred to $S1$ (see Fig. 3.1a) - y = 15 mm - The extent of the surface defect ranges from 10 mm to 22 mm; (b) THz radargram referred to $S2$ (see Fig. 3.1b) - y = 20 mm - The extent of the surface defect ranges from 18 mm to 25 mm.

Foreign body detection

Fig. 3.8 contains THz false colours related to the samples $S3$ and $S4$, shown in Fig. 3.2. Figure 3.8a displays the maximum amplitude of the reflected THz field as a function of the position of the object. In this image, it is possible to distinguish shape and size of the metal as reflects essentially all of the THz radiation, differently from the chocolate. Conversely, Fig. 3.8b shows that the polystyrene sheet inserted in the chocolate is not clearly visible and only its edges can be seen.

Fig. 3.9a shows the THz filtered radargram referring to the chocolate sample containing the metal, mimicking the foreign body (i.e., $S3$). The data has been gathered at y = 11 mm, which correspond to a line where the foreign body is present. In these case, two reflections occur, the first due to the air - chocolate interface, the second due to the chocolate - metal interface. The distance between the contaminant and the surface of the sample has been estimated equal to 1 mm for the sample $S3$. Such distance has been calculated from the ToF formula (see Chapter 2), being known the permittivity ϵ_r of the chocolate cream, and the time, which the THz wave employes to pass through the space between the two interfaces. In fact, it is reasonable to assume that ϵ_r is approximately equal to 3 [87].

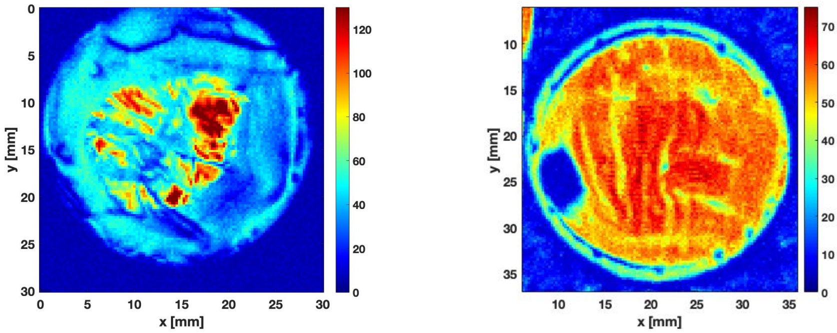

(a) (b)

Figure 3.8. THz False color images; (a) Maximum amplitude of the filtered signal referred to $S3$, shown in 3.2a; (b) Maximum amplitude of the filtered signal referred to $S4$ in 3.2b.

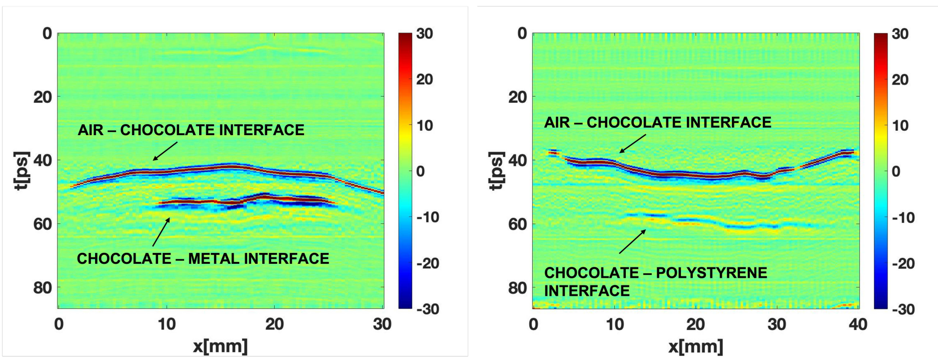

(a) (b)

Figure 3.9. THz radargrams of the samples $S3$ and $S4$. (a) Metal 1 mm deep inside the chocolate; (b) Polysterene 1.5 mm deep inside the chocolate.

Fig. 3.9b shows the THz radargram referred to the chocolate sample containing the polystyrene, as a foreign body (i.e., $S4$). The data has been gathered at y = 10 mm, which corresponds to a line where the contaminant is present. Also in this case, it is possible to distinguish two reflections due to the occurrence of different materials. Herein, the distance between the

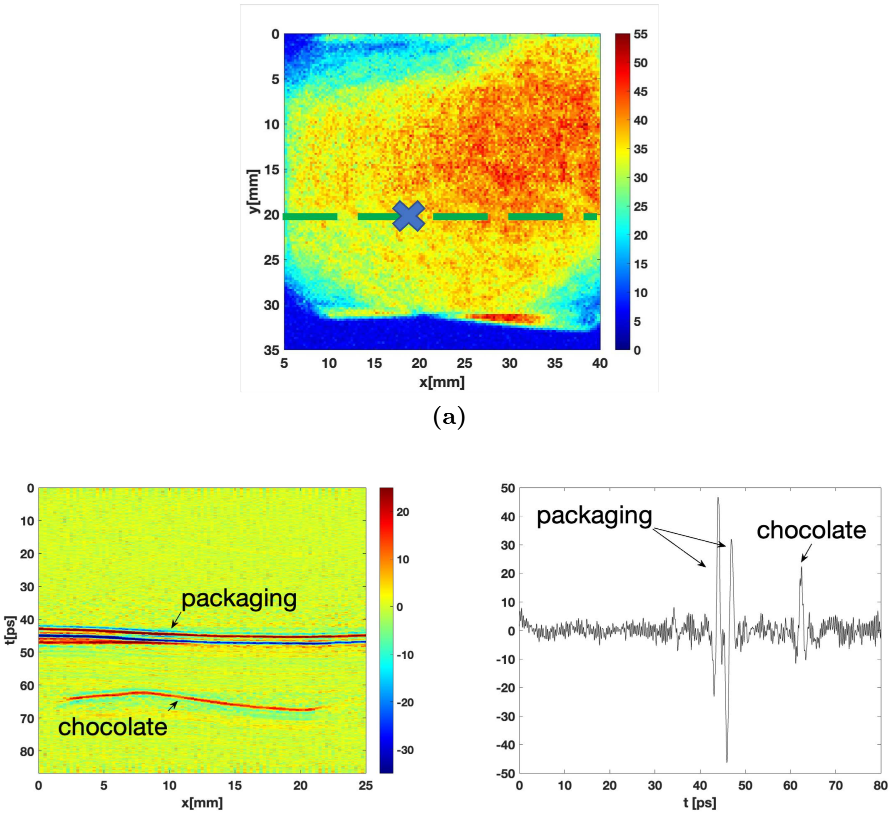

(a)

(b) (c)

Figure 3.10. THz images referred to $S5$, shown in Fig. 3.3d (a) THz false color image; (b) THz filtered radargram - y=20 mm (the green dot line in 3.10a); (c) THz waveform - (20,20) mm (marked with the blue x in 3.10a).

foreign body and the surface of the chocolate cream has been estimated equal to 1.5 mm.

Samples with packaging

Figures 3.10a, 3.11a and 3.12a show the THz false color images referred to the covered samples in Figs. 3.3d-3.3f (i.e., $S5$, $S6$, $S7$). Looking at

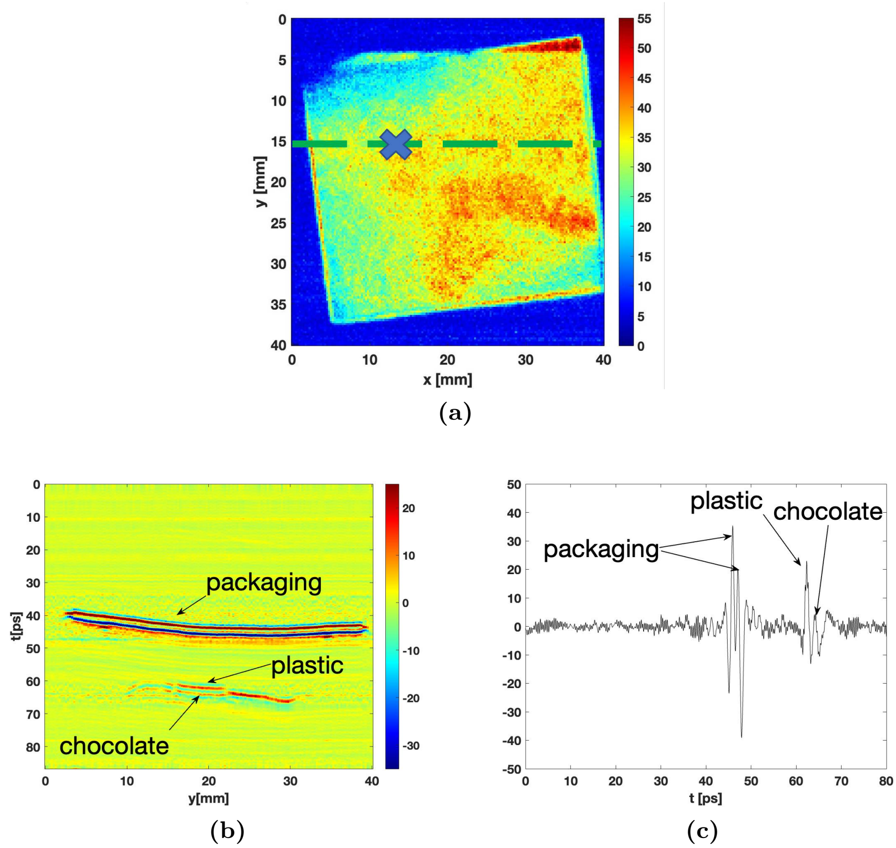

Figure 3.11. THz images referred to $S6$, shown in Fig. 3.3e (a) THz false color image; (b) THz filtered radargram - y=15 mm (the green dot line in 3.11a); (c) THz waveform - (15,15) mm (marked with the blue x in 3.11a).

such images, it emerges that the information about the object under the package is loss. So, THz false-color images, obtained by plotting, point by point, the maximum amplitude of the signal are not informative in the case of packaged products, and other types of investigation are necessary to perform effective inspection of the food product and detect any potential contaminants.

To this end, Fig. 3.10b shows the radargram corresponding to y= 20 mm (i.e., highlighted by the green line in Fig. 3.10a) and referred to the cov-

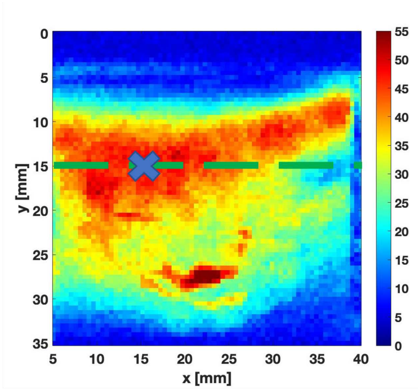

(a)

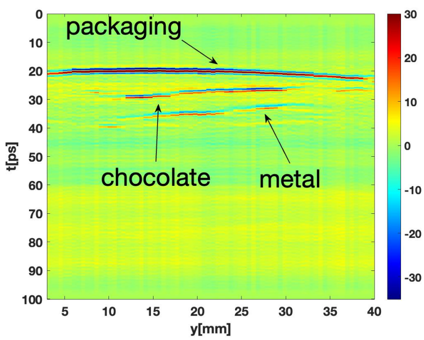

(b)

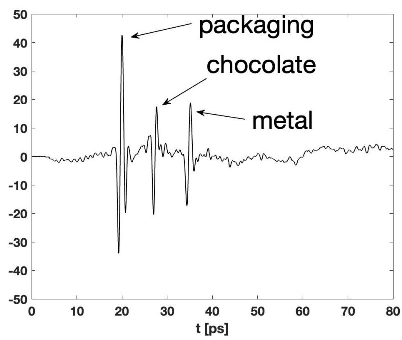

(c)

Figure 3.12. THz images referred to the sample in 3.3f. (a) THz false color image; (b) THz filtered radargram - y=15 mm (the green dot line in 3.12a); (c) THz waveform - (15,15) mm (marked with the blue x in 3.12a).

ered sample $S5$, shown in Fig. 3.3d. By observing Fig. 3.10b, it is possible to distinguish a first reflection due to air-package interface occurring at 42 ps and a second one representing the interface between the air and the chocolate, which occurs at about 62 ps. Instead, Fig. 3.11b, referred to the specimen $S6$ in Fig. 3.3e shows the radargram corresponding to y= 15 mm (i.e., highlighted by the green line in Fig. 3.11a), where occurs three reflections due to the presence of different materials. The first reflection at 40 ps, as in Fig. 3.10b, is related to the presence of the packaging, while

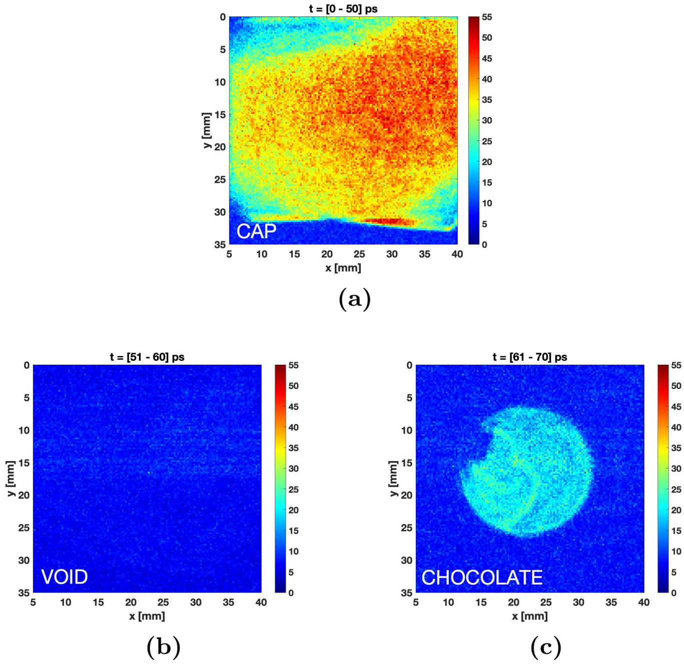

Figure 3.13. Maximum Amplitude of the signal in specific time windows referred to the sample $S5$ in Fig. 3.3d: (a) cap; (b) void between cap and chocolate; (c) chocolate.

the second and the third reflections, at about 60 ps and 65 ps, represent the air-plastic interface and the plastic-chocolate one, respectively. It can be seen that the extent of the defect (i.e., the plastic) is between 9 mm and 22 mm.

Fig. 3.12b shows the THz radargram referred to the case study $S7$ in Fig. 3.3f (corresponding to y= 15 mm, see Fig. 3.12a) where metal was hidden about 1 mm deep inside the chocolate cream. Also in this case, by observing the radargram, it is possible to note the presence of three reflections. The first reflection at 20 ps is related to the presence of the packaging, while the second and the third reflections, at about 26 ps and 37 ps, represent the air-chocolate interface and the chocolate-metal one, respectively.

To corroborate these results, the THz waveforms are shown in Figs. 3.10c,

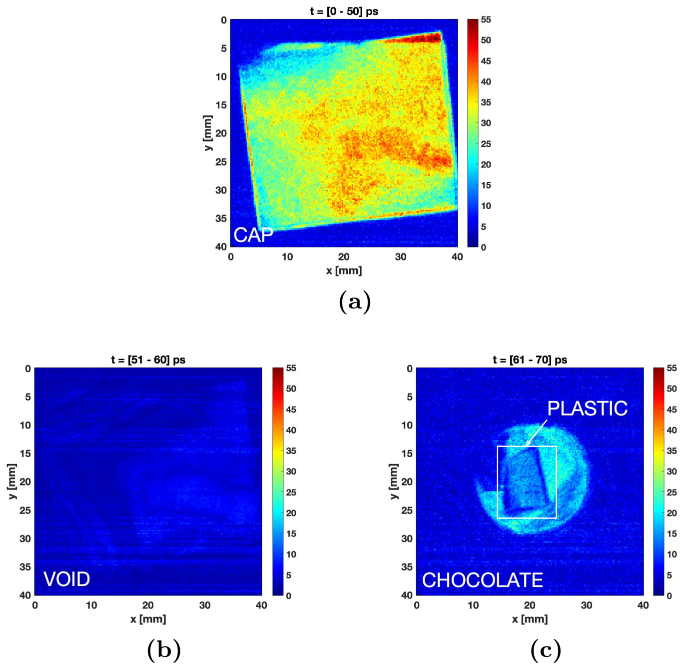

Figure 3.14. Maximum Amplitude of the signal in specific time windows referred to $S6$ in Fig. 3.3e: (a) cap; (b) void between cap and chocolate; (c) chocolate contaminated by plastic.

3.11c, 3.12c corresponding to the blue point highlighted in Figs. 3.10a, 3.11a and 3.12a, respectively. Comparing Fig. 3.10c and Fig. 3.11c, one can see that in both cases the time between the peak of the waveform due to the packaging and the peak due to the reflection of the chocolate is 20 ps, which corresponds to about 3 mm in the air. Figure 3.11c shows also that the reflection due to the plastic occurs 25 ps after the reflection at the air-pack interface, as confirmed by Fig. 3.11b. By observing Fig. 3.12c, it is possible to note that, in this case, the time between the peak of the waveform due to the packaging and the peak due to the reflection of the chocolate is 6 ps, which corresponds to about 1 mm in air.
Further evidence of the ability of detecting the chocolate surface contamination and the inner one is provided by the depth slices show in Figs. 3.13, 3.14 and 3.15, where appropriate time windows have been selected in order

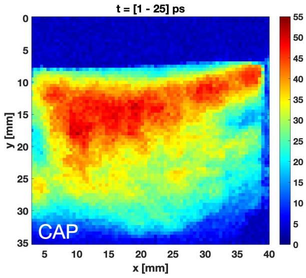

(a)

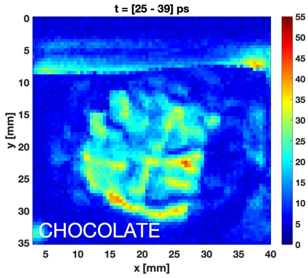

(b)

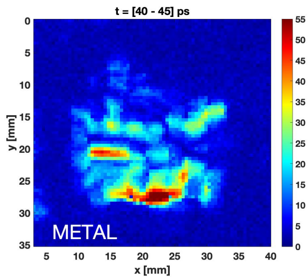

(c)

Figure 3.15. Maximum Amplitude of the signal in specific time windows referred to the sample $S7$ in Fig. 3.3f: (a) cap; (b) chocolate; (c) metal.

to separate the contribution of the first reflections due to the packaging and the ones related to chocolate portions at increasing depths. Figure 3.13a illustrates the amplitude of the signal in the time range of [0-50] ps, as it pertains to the sample depicted in Fig. 3.3d, which represents the packaging. Conversely, Figure 3.13b depicts the void between the cap and the chocolate in the time range [51 - 60] ps, and Fig. 3.13c shows the chocolate cream under the cap, which accounts for the reflection observed in the time range of [61- 70] ps. In addiction, Fig. 3.14a (corresponding to the sample in Fig. 3.3e) shows the signal amplitude in the time window [0-50] ps, which relates to the packaging. On the other hand, Fig. 3.14b shows the void between the cap and the chocolate in the time range [51 - 60] ps, as Fig. 3.13b. Fig. 3.14c illustrates the reflections observed in the time window [61-70] ps, which are caused by the presence of chocolate

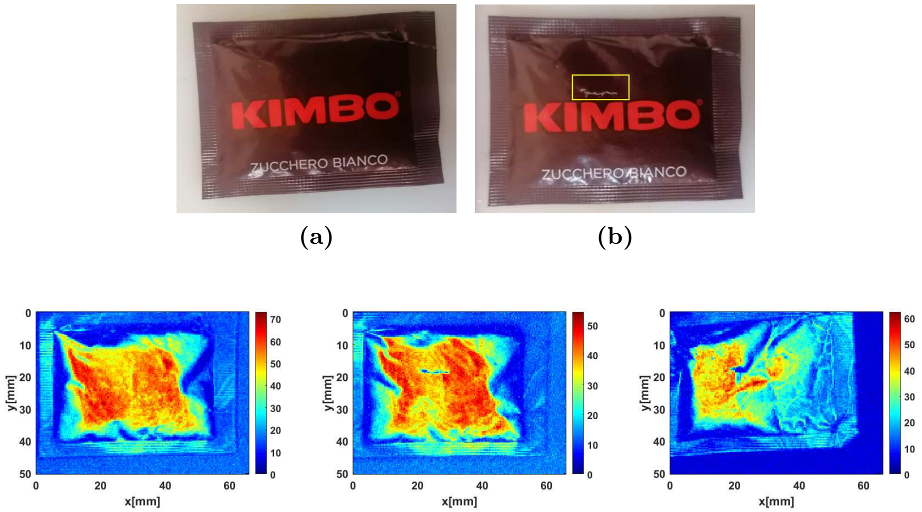

(c) (d) (e)

Figure 3.16. Sugar bags. (a) Photo of a standard packaging; (b) Photo of defect packaging highlighted in the yellow box; (c) THz False color standard packaging; (d) THz False Color defect packaging; (e) THz False color when the sugar has been moved on the left side.

and plastic fragments, whose edges appear in the figure and are enclosed by the white contoured rectangle. Furthermore, Figure 3.15a shows the signal amplitude in the time window [1-25] ps referred to the sample in Fig. 3.3f, wherein only the response of the packaging is considered. Figure 3.15b referring to the intervals [25-39] ps takes into account the contribution related to the chocolate. Finally, the third depth slice in Figure 3.15c is obtained by selecting the time interval [40-45] ps and contains the metal fragment hidden inside the cream.

3.3 A further investigation: Packaging Control

Among the possible applications of THz imaging, a potential area is the detection of production defect in plastic or paper packaging. In this framework, analysis regarding paper packaging defects have been carried out. This section presents the results referred to sugar bags with and without packaging defects. A standard packaging is reported in Fig. 3.16a, while the sachet of sugar in Fig.3.16b is characterized by a surface defect of about 10 mm. The data has been gathered with a 0.4 mm spatial resolution along the x and y axes and a scan area of 65 mm $\times$ 50 mm. Figures 3.16c and 3.16d indicates the ability of THz imaging to represent accurately the surface of the packaging. In particular, the defect of the package has been successfully checked guaranteeing an effective control of quality as shown in Fig. 3.16d. These results allow us to appreciate the diagnostic capabilities of THz technology of detecting packaging defect that could compromise the quality of the food. It is worth pointing out that the sugar is clearly identified under the paper layer in the THz images as shown in Fig. 3.16c and Fig. 3.16d. This indicates that, despite the limits related to the penetration depth of the THz, it is possible, in principle, to investigate the content of the packet. To confirm this observation, Fig. 3.16e shows the THz image of a sachet where the sugar has been moved to the left side. The sugar distribution is clearly distinguishable from the image obtained.

Chapter 4

Non-Destructive Characterization of Magnetic Polymeric Scaffolds

The use of TeraHertz (THz) waves for the non-destructive characterization of Magnetic Scaffolds (MagS) represents an open challenge for the scientific community. MagS are 3D composite materials, in which magnetic nanoparticles (MNPs) are used to load a polymeric matrix. Due to their wide use in various medical applications, there is an increasing demand of advanced techniques for non-destructive quality assessment procedures aimed at verifying the absence of defects and, more generally, dedicated to the characterization of MagS.

This chapter deals with an approach for the characterization of MagS by means of a THz time-domain system used in reflection mode. The proposed data processing approach allows a quantitative characterization of MagS, in terms of their (estimated) thickness and refractive index. Moreover, the proposed procedure allows to identify the areas of the scaffold wherein MNP are mainly concentrated and thus, it gives us information about MNP spatial distribution.

The material presented in the chapter is contained in an article under review on the IEEE Transaction on Terahertz Science and Technology.

4.1 Material

4.1.1 Magnetic Scaffolds

MagS are 3D composite materials, in which iron oxide (Fe_3O_4) MNPs are used to load a polymeric matrix made of poly(ϵ - capprolactone) (PCL).

It is well known that polymer scaffolds used for tissue engineering should possess proper architecture and mechanical properties to support cell adhesion, proliferation, and differentiation [88]. Typical scaffold designs have included meshes and fibers; these designs are chosen because they promote uniform cell distribution, diffusion of nutrients, and the growth of organized cell communities [89]. Therefore, the architecture of a PCL scaffold is made using fibers that are superimposed on each other forming a grid to obtain a solid structure having a certain porosity. The choice of the ideal fiber size and the porosity of the scaffold depends on the proposed function of the scaffold itself [90].

Regarding the process of incorporation of MNP into the polymer matrix, the one used for the analyzed MagS consists of dropping the MNP dispersed in water onto the PCL scaffolds and the deposition occurs under the driving force of an external magnet [58].

4.1.2 Laboratory Case Studies

Polymeric scaffolds produced by 3D Biotek (3D Biotek LLC) have been considered in this study. The set of 3D-Insert are constituted by a 90°-

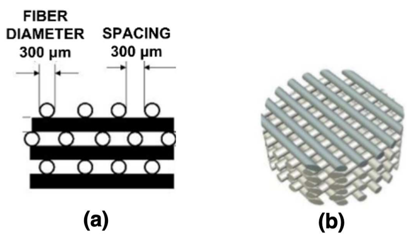

Figure 4.1. (a) 3D-Insert consisting of a 90°-interlaced fiber architecture, with a fiber diameter of 300 μm, spaced by 300 μm. (b) Image of the 3D structure of the scaffold.

interlaced fiber architecture, with a fiber diameter of 300 μm, spaced by 300 μm, resulting in a nominal porosity of about 80% (see Fig. 4.1a). These standard poly-caprolactone (PCL) disks have a 5 mm diameter. A representative image of the 3D structure of the scaffold is shown in Fig. 4.1b. The drop-casting deposition is tuned to obtain different distributions of MNPs in the biomaterial as described in [58]. The four MagS analyzed in this study are shown in Fig. 4.2, where the sample named $0A$ does not contain MNPs and is used as reference.

4.2 Method

4.2.1 Measurement Protocol

The procedure used to carry out the measurements of the Samples under Test (SuT) can be summarized in the following steps.

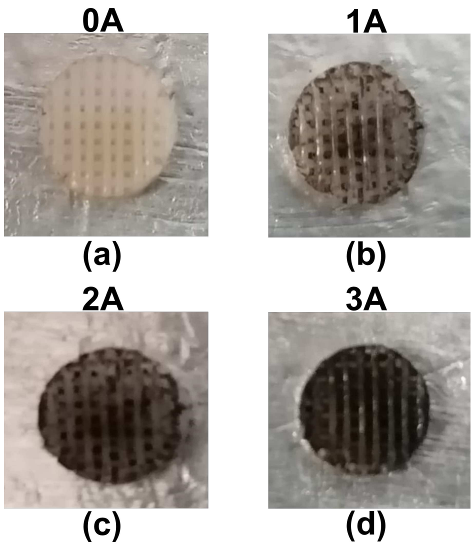

Figure 4.2. Photos of the samples: (a) scaffold without MNPs named sample 0A; (b)-(d) scaffolds with a different amount of MNPs and referred as sample 1A, 2A and 3A, respectively.

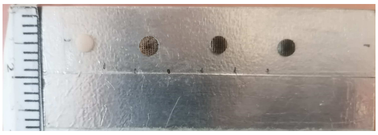

(a)

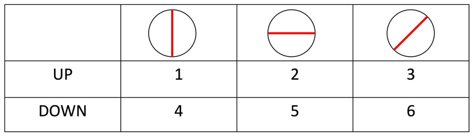

UP	1	2	3
DOWN	4	5	6

(b)

Figure 4.3. (a) Samples placed on a metal plate. (b) Measurement set up; we will refer to the six configurations with numbers from 1 to 6.

1. The samples are placed on a metal plate in order to have a unique temporal and spatial reference (see Fig 4.3a). This choice is useful because the metal totally reflects the signal passing through the sample allowing us to identify the time corresponding to the last peak of the gathered waveforms, due to sample-metal interface (end of the specimens).

2. Six measures are made for each SuT that are numbered from one to six and summarized in Fig. 4.3b. The samples are analyzed by collecting data on both sides (up and down) and with three different fibers orientations (see Fig. 4.4). In particular, the specimens are measured with the fibers oriented as shown in Fig 4.4a (the starting position $\alpha = 0°$, where α is the angle between the fiber shown in red

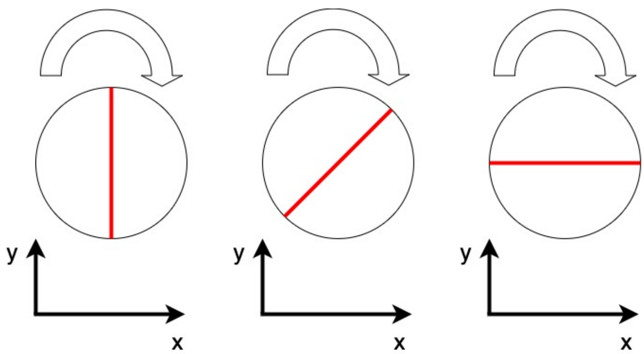

Figure 4.4. Different fibers orientations used to carry out the measurement. (a) Starting position $\alpha = 0°$. (b) Rotaded by 45°. (c) Rotaded by 90°.

in Fig. 4.4 and the y axis), rotated by 45° ($\alpha = 45°$, see Fig. 4.4b) and by 90° ($\alpha = 90°$, Fig. 4.4c), with respect to the initial position.

The measurement protocol consists of six measures for each SuT and this is made because small variations in the results may occur, mainly due to two factors. The first one is the random placement of the sample on the scanning platform of the THz measurement system. The second one is the texture of the sample, which consists of 90° -interlaced fiber architecture, as described in Sec. 4.1.1, that can affect the propagation time of the THz signal within the object. The polymer matrix, as shown in Fig. 4.1, has empty spaces between the fibres, which alters the propagation of the THz signal. Furthermore, the time that the THz signal employs to propagate depends on the mutual position of the fibres, and thus on their orientation with respect to the emitter and the receiver locations.

THz measurements were performed in uncontrolled environment conditions with temperature values in the range 28°C - 30°C and humidity percentages from 30% to 35%. The data were gathered by scanning a 10 mm x 10 mm area with a 0.12 mm spatial offset along x and y axes, which was selected in agreement with the spatial variability of the geometrical features of the investigated samples. The time required to collect each data set was less than 5 minutes, while the processing time was about a couple of minutes. Of course, such a time is not negligible but, it is reasonable for high precision laboratory measurements.

Moreover, the thickness of the samples in Fig. 4.2, say d_m, are shown in Tab 4.1. Such values were measured by means of a manual gauge, having an accuracy of about 10^{-1} mm.

Table 4.1. Thickness of the MagS, d_m, measured with a manual gauge.

Sample	$0A$	$1A$	$2A$	$3A$
$d_m[mm]$	1.55	1.40	1.50	1.30

4.3 Characterization of the MagS

This section is devoted to describe the approach to characterized the MagS, which can be summarized in the following steps:

- Estimation of the thickness (Δ);
- Estimation of the refractive index (η);
- Evaluation of the 2D spatial distribution of the MNPs (MDM);
  - Definition of THz Propagation Delay Map (PDM);
  - Definition of the Magnetization Index (I_m);
  - Definition of THz reference propagation times (t_M, t_{NM});
  - Definition of Magnetization Concentration Mask (MCM);
  - Definition of the Magnetization Distribution Index (I_{md});

The approach is applied to the filtered THz data obtained as described in Chapter 2.

4.3.1 Thickness Estimation

The thickness of the SuT (Δ, in mm), is computed by using the ToF formula, see eq 2.1 in Chapter 2. In particular, it is estimated as the difference between the distance from the emitter/receiver to the metallic surface on which the samples are placed, say d_1, and the distance between the emitter/receiver and the sample surface, i.e., the top of the scaffold, say d_2 (see Fig. 4.5). The distances d_1 and d_2 are computed according to

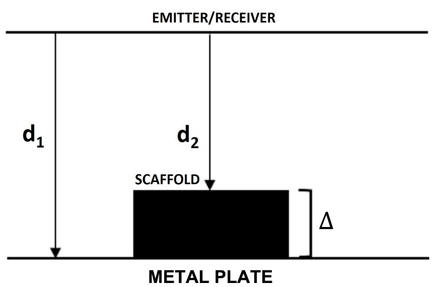

Figure 4.5. d_1 is the distance between the emitter/receiver and the metal plate. d_2 is the distance between the emitter/receiver and the surface of the scaffold. Δ is the thickness of the object.

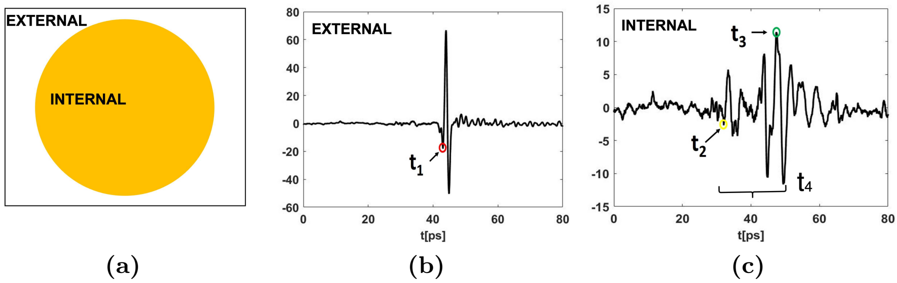

Figure 4.6. (a) Scan Area: external and internal points exploited to derive the averaged A- scans. The yellow circle represents the scaffold. (b) Averaged A Scan from which the value of t_1, highlighted by a red circle, is derived. (c) Averaged A Scan used to derive the value of t_2 and t_3 pointed out by a yellow circle and a green one, respectively. t_4 represents the time that the waveform employs to propagate within the SuT.

the ToF formula (see eq. 2.1 in Chapter 2):

$$d_i = \frac{c \cdot t_i}{2} \tag{4.1}$$

with $i = 1, 2$; where c is the speed of light in the vacuum (m/s) and t_i is the time, in ps, that the waveform employs to propagate from the emitter to the metal plate (t_1) or to the top of the scaffold (t_2) and go back to the receiver.

The time t_1 has been estimated from the A-Scan obtained by averaging the collected waveforms referred to the parts of scanned area that are not covered by the scaffold and it is referred to as external area (see Fig. 4.6a). This A-Scan takes into account the waveforms collected outside the sample, and t_1 is identified as the first minimum, calculated going back in time, starting from the peak of the reflected signal due to air-metal interface (see Fig. 4.6b).

The time t_2 is estimated from the A-Scan obtained by averaging the collected waveforms of the scanned area intercepting the scaffold, and referred to as internal area (see Fig. 4.6a). In particular, t_2 is identified as the first minimum value, just before the peak due to air-sample interface, see Fig. 4.6c. Once the two distances have been estimated, it is possible to estimate the thickness of the scaffold by simply subtracting $\Delta = d_1 - d_2$.

4.3.2 Refractive Index Estimation

The second step involves the identification of the refractive index (η) of the analyzed samples and allows the characterization of the SuT from an EM point of view. Considering that MagS is not homogeneous, by the term refractive index I mean the effective refractive index. This value, once again, is derived from the ToF formula (Chapter 2, eq. 2.1). Let v be the EM wave propagation velocity into the object, it is given by $v = \frac{c}{\eta}$. Hence, the refractive index η is derived as :

$$\eta = \frac{c \cdot t_4}{2 \cdot \Delta} \tag{4.2}$$

where Δ is the estimated thickness of the object and t_4 represents the time that the waveform employs to propagate within the SuT. This time is given by the difference between the time instant t_3 corresponding to the peak of the reflected wave due to the object-metal interface and the time instant t_2 corresponding to the peak referred to top face of the scaffold (see Fig. 4.6c).

4.3.3 MNPs Spatial Distribution Estimation

To extract the spatial distribution of MNPs in the polymeric matrix, the THz Propagation Delay Map (PDM) of the SuT is first derived. PDM is a 2D image representing the propagation time delay of the THz wave due to the presence of MNPs into the scaffold. Such map is a 2D differential image obtained by subtracting, for each pixel, the propagation time referred to the sample under test and a reference propagation time (t_{NM}) computed by considering an ideal homogeneous scaffold having the same thickness of the surveyed one but being without MNPs. The propagation time referred to the SuT is retrieved from the measured data, for each pixel of the scanned area intercepting the scaffold, as the value of the time interval occurring between the time instant of the peak due to the scaffold top face (air-scaffold interface), and the time instant of the peak due to the scaffold bottom face (scaffold-metal plate interface). Of course, the duration of this time range depends on the material wherein the signal propagation occurs and it is, therefore, affected by the presence and the amount of MNPs. The reference propagation time (t_{NM}) is the propagation time referred to a scaffold having the same thickness of the scaffold under test and the refractive index estimated for the sample $0A$ in Fig. 4.2, i.e., the scaffold without MNPs. Then, the pixels of the scaffold wherein there are MNPs are detected from the PDM as the ones different from zero. The PDM allows the estimate of a Magnetization Index (I_m), synthetically encoding the amount of MNPs present in the SuT (with respect to a homogeneous reference). The I_m value is given by the ratio between the number of pixels containing MNPs and the total number of pixels discretizing the scanning area and intercepting the scaffold, i.e. the number P of pixels belonging to the internal area (see Fig. 4.6a);

$$I_m = \frac{\sum_{i,j=1}^{N,M}(x_{i,j} > 0)}{P} \tag{4.3}$$

being $x_{i,j}$ the pixel considering and $N \times M$ the dimension of the image.

Furthermore, the areas where the MNP are mainly concentrated are retrieved by introducing a threshold T defined by the difference between the times of flight of the reference scaffold without MNPs (t_{NM}) and the time of flight for the one homogeneously loaded with MNPs (t_M). This latter is derived using the ToF formula (Eq. 2.1) where Δ is the thickness of the SuT and v is the EM wave velocity in an object having the refractive index η estimated for the SuT. The value T is used to threshold the PDM and to obtain a binary magnetization map, which we will refer to as Magnetization Concentration Mask (MCM). In this map, the pixels where the propagation time is larger than T are set to one, being estimated as the pixel where the presence of the MNPs significantly affects the THz signal propagation through the sample. The MCM allows the estimate of a Magnetization Distribution Index (I_{md}), which accounts for the areas of the scaffolds where the MNPs are mostly concentrated (with respect to a homogeneous distribution of MNPs in the polymeric matrix). The I_{md} value has been calculated as the ratio between the number of pixels where the propagation time is larger than T and the total number of pixels P:

$$I_{md} = \frac{\sum_{i,j=1}^{N,M}(x_{i,j} > T)}{P} \tag{4.4}$$

Table 4.2. t_1, t_2 and t_3 in ps for all the measurement set.

	$t_1[ps]$				$t_2[ps]$				$t_3[ps]$			
Measurement	$0A$	$1A$	$2A$	$3A$	$0A$	$1A$	$2A$	$3A$	$0A$	$1A$	$2A$	$3A$
1	42.9	41.3	42.0	43.7	32.0	31.7	32.1	34.8	48.4	46.9	47.7	49.2
2	43.3	41.4	41.3	41.0	32.6	32.0	31.4	32.1	48.9	46.8	47.1	46.6
3	41.2	41.2	42.1	42.1	30.6	31.5	32.0	33.2	47.0	46.7	47.8	47.4
4	41.6	41.9	42.8	42.5	30.6	32.2	32.8	33.7	47.3	47.2	48.6	48.2
5	43.3	41.4	41.2	42.3	32.7	31.2	31.2	33.5	48.9	46.7	46.8	47.6
6	42.4	41.7	42.4	44.6	31.7	32.0	32.4	35.7	48.2	47.0	48.5	49.8

being $x_{i,j}$, N and M defined as above.

Finally, the 2D MNPs Distribution Map (MDM) is retrived by multiplying pixel by pixel the binary MCM and the map of the filtered THz signal amplitude (i.e., THz False colors image). This image is normalized to its maximum value and allows to distinguish the areas of the SuT where MNPs are mostly concentrated and to detect how the distribution of the MNPs changes along x and y directions.

4.4 THz results of the Case Studies

The results obtained for the MagS introduced in Sec. 4.1.2 (Fig. 4.2) using the procedures detailed in Sec. 4.3 are reported in this section.

Tab. 4.2 shows the time t_1, and the values t_2 and t_3, derived from the A-scans described in Sec. 4.3.1 and 4.3.2, for the six measurement set up (see Fig. 4.3b). These values were used to derive the thickness Δ and refractive index η shown in Tab. 4.3, for measurement 1 to 6. In addition, for each sample the results of Δ and η were averaged: 1) M_{up} contains the average values of measurements 1-2-3 (i.e., sample upwards with three different fibre orientations: $\alpha = 0°, 90°, 45°$); 2) M_{down} contains the average of measurements 4-5-6 (i.e., sample downwards with three different fibre orientations: $\alpha = 0°, 90°, 45°$); 3) M_{tot} contains the average of all six measurements.

Table 4.4 compares the average thickness values derived from THz data

Table 4.3. Δ and η values for each measurement and their averages M_{up}, M_{down}, M_{tot}

	$0A$		$1A$		$2A$		$3A$	
Measurement	Δ[mm]	η	Δ[mm]	η	Δ[mm]	η	Δ[mm]	η
1	1.62	1.52	1.47	1.56	1.50	1.56	1.34	1.61
2	1.61	1.52	1.41	1.57	1.50	1.58	1.34	1.61
3	1.59	1.54	1.45	1.57	1.50	1.58	1.33	1.60
4	1.65	1.52	1.45	1.55	1.49	1.59	1.32	1.65
5	1.58	1.54	1.45	1.55	1.50	1.57	1.32	1.60
6	1.60	1.55	1.45	1.55	1.51	1.60	1.34	1.58
M_{up}	1.61	1.53	1.44	1.57	1.50	1.57	1.34	1.61
M_{down}	1.61	1.54	1.45	1.55	1.50	1.59	1.33	1.61
M_{tot}	1.61	1.53	1.45	1.56	1.50	1.58	1.33	1.61

(Δ), referred to all the six measurements (M_{tot}), with those measured by means of a manual gauge (d_m), having an accuracy of about 10^{-1} mm. Table 4.5 shows at its first row the THz propagation times of the reference samples without MNPs (t_{NM}) exploited to derive the PDMs in Fig. 4.7, referring to the sample $1A$, $2A$ and $3A$.

The second row of Tab. 4.5 contains the instant times t_M referred to the scaffolds homogeneously loaded with MNPs, that allow to obtain the threshold T (see the third row of Tab. 4.5) used to retrieve the MCMs shown in Fig. 4.8b, Fig. 4.9b and Fig. 4.10b. Tab. 4.6. contains the Magnetization Index (I_m) and the Magnetization Distribution Index (I_{md}).

Table 4.4. Thickness of the magnetic scaffolds: d_m is the value measured with a manual gauge - Δ is the averaged thickness estimated for all the measurement set.

Sample	$0A$	$1A$	$2A$	$3A$
$d_m[mm]$	1.55	1.40	1.50	1.30
$\Delta[mm]$	1.61	1.45	1.50	1.33

Table 4.5. t_M, t_{NM} and $T[ps]$ calculated considering the average Δ and the average η for all the six measurement set.

Sample	$1A$	$2A$	$3A$
$t_{NM}[ps]$	14.70	15.30	13.56
$t_M[ps]$	15.00	15.80	14.28
$T[ps]$	0.30	0.50	0.72

Table 4.6. I_m and I_{md} for the MagS.

Sample	$0A$	$1A$	$2A$	$3A$
I_m	0	0.88	0.97	0.99
I_{md}	0	0.14	0.27	0.48

The 2D MNPs Distribution Map (MDM) are shown in Fig. 4.8c, Fig. 4.9c and Fig. 4.10c compared with the optical image of the corresponding MagS.

4.5 Discussion

THz data referred to the six measurement setups shown in Tab. 4.2 have been used to estimate Δ and η, and the results are presented in Tab. 4.3.
As shown in Tab. 4.3, small variations in the results occur due to the different position of the MagS texture, which is made by 90°-shifted highly porous mesh, on the scanning platform of the THz system. The texture of the MagS and the presence of empty spaces between the fibers, affect the propagation time, which depends on the mutual position of the fibers and on their orientation with respect to the emitter and the receiver locations.

There are also small variations in the results of Δ and η, as shown from the row 1 to 6 in Tab. 4.3, due to the fact that such values are computed from the instant times t_1, t_2 and t_3 (see Sec. 4.3.1 and 4.3.2).

Tab. 4.3 shows the estimated values of Δ and η for the single measure

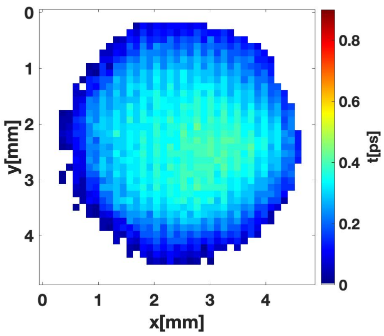

(a)

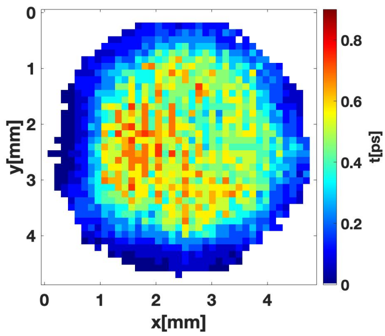

(b)

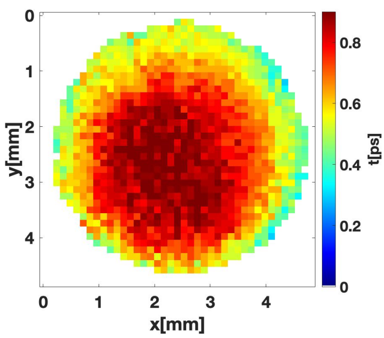

(c)

Figure 4.7. Propagation Delay Maps (PDMs). (a) 1A. (b) 2A. (c) 3A.

(a)

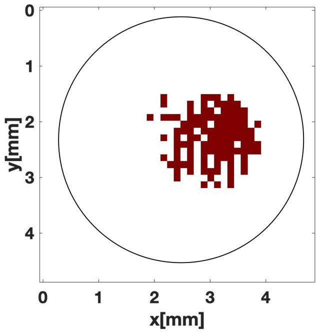

(b)

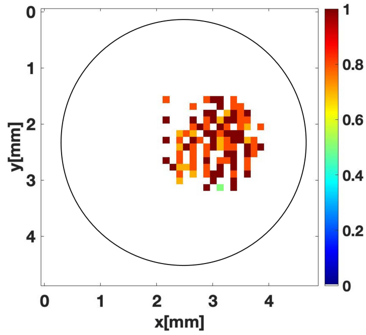

(c)

Figure 4.8. (a) Photograph of the MagS 1A. (b) MCM 1A. (c) 2D MDM 1A.

(from row 1 to 6) and for the averaged measures. The results do not differ significantly each other if we consider an approximation to the first digit. Therefore, they suggest that a single measurement could be sufficient, even if the average of three measurements, with the sample up or down, or six measurements (i.e., MagS up and down) increases the robustness of the MagS characterization.

The effectiveness of the procedures described in Sec 4.3.1 is demonstrated by comparing the averaged values estimated from the THz data Δ (i.e., referred to M_{tot}), and the values measured with the manual gauge d_m with an accuracy of about 10^{-1} mm. The results in Tab. 4.4 demonstrate that the proposed method gives good results considering the accuracy of the manual gauge. It is worth noting that, as shown in Tab. 4.3, the sample without MNPs (i.e., $0A$) has the lowest η value, as expected, while

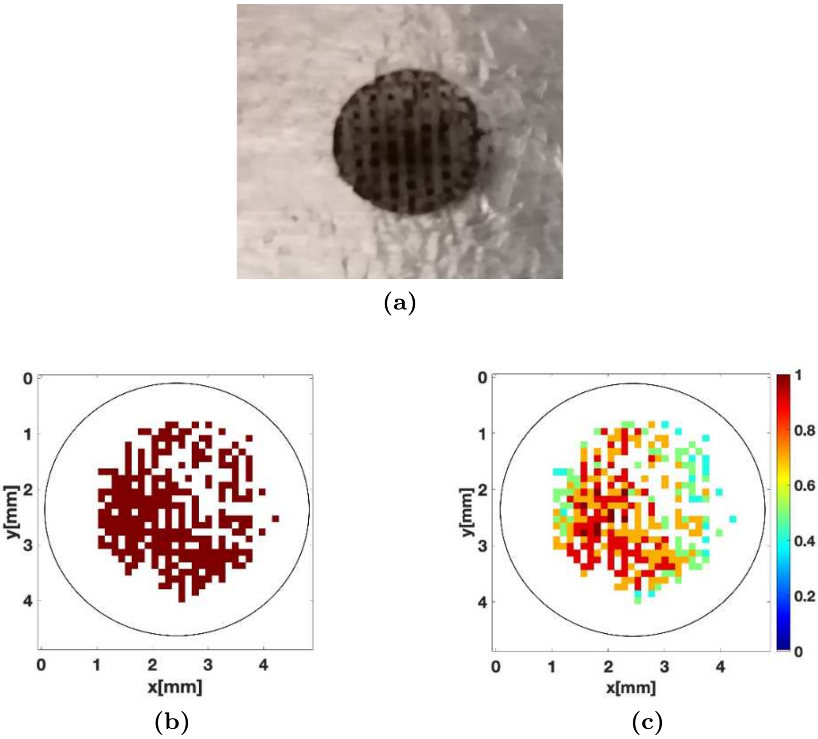

Figure 4.9. (a) Photograph of the MagS 2A. (b) MCM 2A. (c) 2D MDM 2A.

the other samples show an increasing trend. In particular, sample $3A$ is characterized by the highest η value and this is compliant with the largest amount of MNPs.

The PDMs shown in Fig. 4.7 contain the THz propagation delay, in ps, introduced by the presence of MNP and allow the introduction of the magnetization indices, I_m, shown in the first row of Tab. 4.6. The obtained results state, as foreseeable, that when the amount of MNP increases also η increases, while I_m approaches to 1. Moreover, the results referred to I_{md} (see second row of Tab. 4.6) show that higher I_{md} values correspond to larger areas where MNPs are concentrated, which is confirmed by both the MCM and the picture of the MagS.

Looking at the photo of sample $1A$ in Fig. 4.8a, it is possible to note that there is a higher MNP concentration in the center, as confirmed by

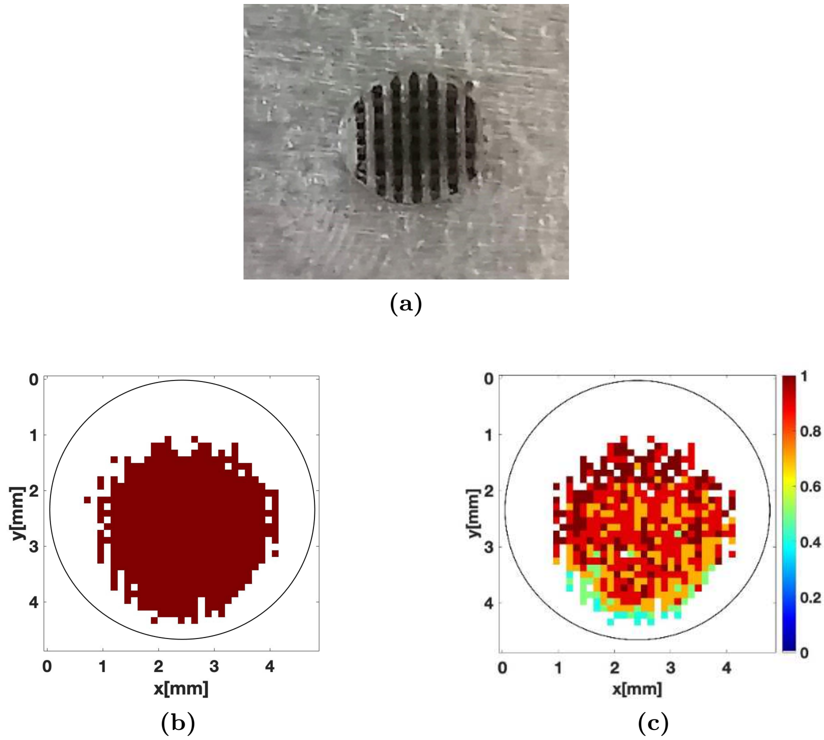

Figure 4.10. (a) Photograph of the MagS 3A. (b) MCM 3A. (c) 2D MDM 3A.

the MCM in Fig. 4.8b. Similarly, for the sample $2A$, the MNPs are present in lower amounts at the edges, while they are present in higher amounts in the other parts of the scaffolds, as shown in the photo of the specimen in Fig 4.9a and confirmed by the MCM (see Fig. 4.9b). Finally, sample $3A$ appears to have a higher MNP concentration, as confirmed both by the photography in Fig. 4.10a as well as by our results in Fig. 4.10b

The 2D maps of MNP distribution in Fig. 4.8c, Fig. 4.9c and Fig. 4.10c, each normalized to its maximum value, allow us to see how the MNP distribution changes along x and y axis in the areas where they are present in greater amounts. Fig 4.8c shows that MNP are distributed almost homogeneously in the sample $1A$, but they are in a limited part of the scaffold. Conversely, the figure 4.9c referring to the sample 2A, shows a larger presence of MNPs in the central region (x ranging from 1.5 to 3 mm and y between 1 and 3.5 mm). Sample $3A$ (see Fig. 4.10c), which contains the largest amount of MNPs, has a homogeneous distribution along the x and y axes like sample $1A$, and in this case MNP fill almost the entire scaffold.

Chapter 5

Conclusions

5.1 Conclusions

This thesis has dealt with the exploitation of THz imaging technologies to non-invasive inspect and characterize materials of interest in food and biomedical industries.
As for the non-destructive inspection of food products, 2D THz false color images allow for effective identification of surface defects and contaminants by exploiting the different reflectivity of the materials when they are illuminated by THz radiation. However, 2D THz false color images are not informative in the case of packaged products, and other types of investigation are necessary to perform effective inspection of the food product and detect any potential contaminants. To this end, the analysis of THz radargrams gathered in a number of controlled experiments has demonstrated the capability of THz wave of passing through a wide variety of packaging materials. Provided the THz signal is properly filtered, such a capability allows to localize the presence of foreign bodies and to investigate various layer contained within the sample. Further evidence of the ability of detecting contaminants in food samples is provided by THz depth slices, where the selection of appropriate time windows allows to separate different layers of the objects under test at increasing depths.
These studies corroborate that THz imaging can be regarded as an alternative or complementary modality for the NDI of food products.
Regarding the first research activity, this thesis makes a contribution to the

THz community by providing a procedure that enhance the capabilities of THz imaging to solve practical issues in NDI (such as the developing of ad-hoc measurement protocol, procedures aims to remove environmental noise from the data, imaging techniques which allow to effective inspection of the food samples). As an example, a performance assessment of THz capabilities to inspect chocolate cream samples is provided.

The second research activity proposed a THz imaging strategy for non-destructive inspection of composite materials, particularly MagS, commonly used in biomedical applications. This thesis provides a novel method for non-destructive characterization of MagS, based on THz Imaging, which has not been attempted before.

Notably, THz imaging, compared to the other techniques used to study MagS, enables non-destructive characterization without the use of ionizing radiation, as in MicroCTs, and with a less complex and laborious measurement procedure (i.e., the samples were simply placed on the scanning area of the THz system) compared to other techniques such as SEM and TEM. The proposed approach enables a quantitative characterization of the material's thickness (Δ) and refractive index (η) along with the introduction of two reference propagation times. The procedure allowed us to define two indices, the magnetization index, I_m, and the magnetization distribution index, I_{md}, which take into account the areas where MNPs occur and gave us information about the region where they are present in greater quantities, respectively.

Regarding the second research activity, this thesis makes a contribution by developing advanced THz imaging approaches which could be relevant to materials scientists, bioengineers and clinicians who want to fabricate, characterize and use MagS as multifunctional tools for tissue engineering, drug delivery and hyperthermia. Furthermore, the results presented in this thesis support the possibility of using THz technology to improve MagS fabrication techniques.

5.2 Perspectives and future trends

The potential applications of THz imaging in the fields of food and biomedical industry are being explored continuously. It is clear that there is still a long way to go before this technology can be applied in industrial

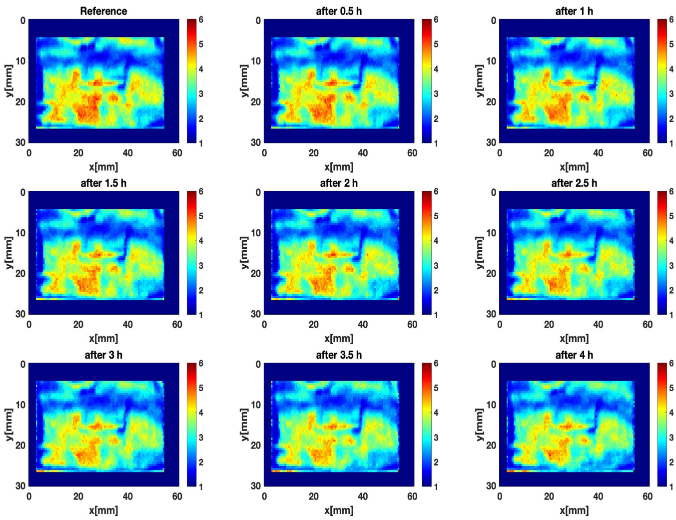

Figure 5.1. Maps of permittivity values of unbaked puff pastry. The first map is the reference one, the subsequent ones showing the material's THz behavior when left at room temperature. Data was collected at 30-minute intervals. The maps reveal that certain areas of the pastry gradually dry out over time, resulting in a lower permittivity value.

processes, although the effectiveness of THz imaging has been demonstrated for a large number of issues. In fact, the costs of THz instrumentation are still very high, there are limits in the penetration depth that can be investigated and the process is time consuming. So future research is needed to develop fast and economical THz systems through the implementation of compact and more efficient instrumentation. Contributions should be made to the development of a global reliable and standardized database in order to improve the quantitative analysis, material identification and to simplify the prediction and detection processes. Last, but not least and more related to the scope of this work, there is significant need for further development of more powerful signal processing routines to allow for real-time analysis of THz time-domain signals. Despite the limitations, THz imaging is establishing itself as a powerful tool for non-destructive inspection, and for the next future its use is expected to be

considered in a wide range of surveys and become more and more a consolidated technology.
The presented studies have opened up several challenges that are still ongoing. For example, a promising area of research is the study of the variation of the electromagnetic properties of doughs as a function of humidity. This topic is relevant as for many types of raw dough, the water content is a fundamental parameter for quality evaluation. To this end, feasibility studies were conducted on a sample of unbaked puff pastry. Figure 5.1 shows nine maps of permittivity values of unbaked puff pastry. The first map is the reference one, the subsequent ones showing the material's THz behavior when left at room temperature. Data was collected at 30-minute intervals. The maps reveal that certain areas of the pastry gradually dry out over time, resulting in a lower permittivity value.
These preliminary results have been encouraging and open up interesting scenarios in the field of quality dough inspection and materials characterization.
Concerning the characterization of MagS, the proposed study addressed opens new challenges aimed at 3D characterization of the MagS (i.e., evaluation of the volumetric distribution of the MNPs in the scaffold) which would allow estimation of the concentration of the MNPs in the polymer matrix.

Bibliography

[1] DM Mittleman, M Gupta, Ramesh Neelamani, RG Baraniuk, JV Rudd, and M Koch, "Recent advances in terahertz imaging," *Applied Physics B*, vol. 68, pp. 1085–1094, 1999.

[2] Egor V Yakovlev, Kirill I Zaytsev, Irina N Dolganova, and Stanislav O Yurchenko, "Non-destructive evaluation of polymer composite materials at the manufacturing stage using terahertz pulsed spectroscopy," *IEEE Transactions on Terahertz science and Technology*, vol. 5, no. 5, pp. 810–816, 2015.

[3] Ping Ye, Qinghao Meng, Guoyang Wang, Haiyun Huang, Yizhou Yang, Bo Su, and Cunlin Zhang, "Terahertz spectroscopic detection of amino acid molecules under magnetic field," *Heliyon*, vol. 8, no. 11, pp. e11414, 2022.

[4] Ghanshyam Singh, *Terahertz antenna technology for imaging and sensing applications*, Springer, 2021.

[5] Daniel J Bradley, Arthur JF Durrant, F O'Neill, and B Sutherland, "Picosecond pulses from mode-locked dye lasers," *Physics Letters A*, vol. 30, no. 9, pp. 535–536, 1969.

[6] DH Auston, AM Glass, and AA Ballman, "Optical rectification by impurities in polar crystals," *Physical Review Letters*, vol. 28, no. 14, pp. 897, 1972.

[7] KH Yang, PL Richards, and YR Shen, "Generation of far-infrared radiation by picosecond light pulses in linbo3," *Applied Physics Letters*, vol. 19, no. 9, pp. 320–323, 1971.

[8] DH Auston, AM Johnson, PR Smith, and JC Bean, "Picosecond optoelectronic detection, sampling, and correlation measurements in amorphous semiconductors," *Applied Physics Letters*, vol. 37, no. 4, pp. 371–373, 1980.

[9] D Grischkowsky, Søren Keiding, Martin Van Exter, and Ch Fattinger, "Far-infrared time-domain spectroscopy with terahertz beams of dielectrics and semiconductors," *JOSA B*, vol. 7, no. 10, pp. 2006–2015, 1990.

[10] X-C Zhang, Y Jin, and XF Ma, "Coherent measurement of thz optical rectification from electro-optic crystals," *Applied physics letters*, vol. 61, no. 23, pp. 2764–2766, 1992.

[11] L Xu, X-C Zhang, and DH Auston, "Terahertz beam generation by femtosecond optical pulses in electro-optic materials," *Applied Physics Letters*, vol. 61, no. 15, pp. 1784–1786, 1992.

[12] Binbin B Hu and Martin C Nuss, "Imaging with terahertz waves," *Optics letters*, vol. 20, no. 16, pp. 1716–1718, 1995.

[13] Daniel M Mittleman, Rune H Jacobsen, and Martin C Nuss, "T-ray imaging," *IEEE Journal of selected topics in quantum electronics*, vol. 2, no. 3, pp. 679–692, 1996.

[14] website, "https://www.advantest.com/products/terahertz-imaging," .

[15] website, "https://teraview.com," .

[16] website, "https://investor.emcore.com/news-releases/news-release-details/emcore-introduces-portable-terahertz-spectrometer," .

[17] website, "https://terasense.com," .

[18] P Knobloch, C Schildknecht, T Kleine-Ostmann, M Koch, S Hoffmann, M Hofmann, E Rehberg, M Sperling, K Donhuijsen, G Hein, et al., "Medical THz imaging: an investigation of histo-pathological samples," *Physics in Medicine & Biology*, vol. 47, no. 21, pp. 3875, 2002.

[19] Danielle M Charron, Katsuhiro Ajito, Jae-Young Kim, and Yuko Ueno, "Chemical mapping of pharmaceutical cocrystals using terahertz spectroscopic imaging," *Analytical Chemistry*, vol. 85, no. 4, pp. 1980–1984, 2013.

[20] John F Federici, Brian Schulkin, Feng Huang, Dale Gary, Robert Barat, Filipe Oliveira, and David Zimdars, "THz imaging and sensing for security applications—explosives, weapons and drugs," *Semiconductor Science and Technology*, vol. 20, no. 7, pp. S266, 2005.

[21] Ilaria Catapano and Francesco Soldovieri, "A data processing chain for terahertz imaging and its use in artwork diagnostics," *Journal of Infrared, Millimeter, and Terahertz Waves*, vol. 38, pp. 518–530, 2017.

[22] Douglas T Petkie, Izaak V Kemp, Carla Benton, Christopher Boyer, Lindsay Owens, Jason A Deibel, Christopher D Stoik, and Matthew J Bohn, "Nondestructive terahertz imaging for aerospace applications," in *Millimetre Wave and Terahertz Sensors and Technology II*. SPIE, 2009, vol. 7485, pp. 62–70.

[23] Swen Koenig, Daniel Lopez-Diaz, Jochen Antes, Florian Boes, Ralf Henneberger, Arnulf Leuther, Axel Tessmann, René Schmogrow, David Hillerkuss, Robert Palmer, et al., "Wireless sub-thz communication system with high data rate," *Nature photonics*, vol. 7, no. 12, pp. 977–981, 2013.

[24] Baobin Liu and Wei Zhou, "The research of metal detectors using in food industry," in *Proceedings of 2011 International Conference on Electronics and Optoelectronics*. IEEE, 2011, vol. 4, pp. V4–43.

[25] Hildur Einarsdóttir, Monica Jane Emerson, Line Harder Clemmensen, Kai Scherer, Konstantin Willer, Martin Bech, Rasmus Larsen, Bjarne Kjær Ersbøll, and Franz Pfeiffer, "Novelty detection of foreign objects in food using multi-modal x-ray imaging," *Food Control*, vol. 67, pp. 39–47, 2016.

[26] Ronald P Haff and Natsuko Toyofuku, "X-ray detection of defects and contaminants in the food industry," *Sensing and Instrumentation for Food Quality and Safety*, vol. 2, no. 4, pp. 262–273, 2008.

[27] Mikkel Schou Nielsen, Torsten Lauridsen, Lars Bager Christensen, and Robert Feidenhans, "X-ray dark-field imaging for detection of foreign bodies in food," *Food Control*, vol. 30, no. 2, pp. 531–535, 2013.

[28] Wenbo Wang and Jitendra Paliwal, "Near-infrared spectroscopy and imaging in food quality and safety," *Sensing and instrumentation for food quality and safety*, vol. 1, pp. 193–207, 2007.

[29] Chun-Chieh Yang, Moon S Kim, Sukwon Kang, Byoung-Kwan Cho, Kuanglin Chao, Alan M Lefcourt, and Diane E Chan, "Red to far-red multispectral fluorescence image fusion for detection of fecal contamination on apples," *Journal of Food Engineering*, vol. 108, no. 2, pp. 312–319, 2012.

[30] Y. Lee, S. Choi, S. Han, D. Woo, and H. S. Chun, "Detection of foreign bodies in foods using continuous wave terahertz imaging," *Journal of food protection*, vol. 75, no. 1, pp. 179–183, 2012.

[31] K. Wang, D. Sun, and H. Pu, "Emerging non-destructive terahertz spectroscopic imaging technique: Principle and applications in the agri-food industry," *Trends in Food Science & Technology*, vol. 67, pp. 93–105, 2017.

[32] Paula IP Soares, Joana Romão, Ricardo Matos, Jorge Carvalho Silva, and João Paulo Borges, "Design and engineering of magneto-responsive devices for cancer theranostics: Nano to macro perspective," *Progress in Materials Science*, vol. 116, pp. 100742, 2021.

[33] Omid Sedighi, Amirhossein Alaghmandfard, Maziar Montazerian, and Francesco Baino, "A critical review of bioceramics for magnetic hyperthermia," *Journal of the American Ceramic Society*, vol. 105, no. 3, pp. 1723–1747, 2022.

[34] Matteo Bruno Lodi, Alessandro Fanti, Andrea Vargiu, Maurizio Bozzi, and Giuseppe Mazzarella, "A multiphysics model for bone repair using magnetic scaffolds for targeted drug delivery," *IEEE Journal on Multiscale and Multiphysics Computational Techniques*, vol. 6, pp. 201–213, 2021.

[35] Silke Behrens, "Preparation of functional magnetic nanocomposites and hybrid materials: recent progress and future directions," *Nanoscale*, vol. 3, no. 3, pp. 877–892, 2011.

[36] Simone Sprio, Elisabetta Campodoni, Monica Sandri, Lorenzo Preti, Tobias Keppler, Frank A Müller, Nicola M Pugno, and Anna Tampieri, "A graded multifunctional hybrid scaffold with superparamagnetic ability for periodontal regeneration," *International journal of molecular sciences*, vol. 19, no. 11, pp. 3604, 2018.

[37] Yuhui Li, Guoyou Huang, Xiaohui Zhang, Baoqiang Li, Yongmei Chen, Tingli Lu, Tian Jian Lu, and Feng Xu, "Magnetic hydrogels and their potential biomedical applications," *Advanced Functional Materials*, vol. 23, no. 6, pp. 660–672, 2013.

[38] Matteo Bruno Lodi, Alessandro Fanti, Giacomo Muntoni, and Giuseppe Mazzarella, "A multiphysic model for the hyperthermia treatment of residual osteosarcoma cells in upper limbs using magnetic scaffolds," *IEEE Journal on Multiscale and Multiphysics Computational Techniques*, vol. 4, pp. 337–347, 2019.

[39] R De Santis, A Gloria, T Russo, U d'Amora, S Zeppetelli, C Dionigi, A Sytcheva, T Herrmannsdörfer, V Dediu, and L Ambrosio, "A basic approach toward the development of nanocomposite magnetic scaffolds for advanced bone tissue engineering," *Journal of Applied Polymer Science*, vol. 122, no. 6, pp. 3599–3605, 2011.

[40] M Bañobre-López, Y Piñeiro-Redondo, R De Santis, A Gloria, L Ambrosio, Anna Tampieri, V Dediu, and J Rivas, "Poly (caprolactone) based magnetic scaffolds for bone tissue engineering," *Journal of applied physics*, vol. 109, no. 7, pp. 07B313, 2011.

[41] Jung-Ju Kim, Rajendra K Singh, Seog-Jin Seo, Tae-Hyun Kim, Joong-Hyun Kim, Eun-Jung Lee, and Hae-Won Kim, "Magnetic scaffolds of polycaprolactone with functionalized magnetite nanoparticles: physicochemical, mechan-

ical, and biological properties effective for bone regeneration," *Rsc Advances*, vol. 4, no. 33, pp. 17325–17336, 2014.

[42] Azam Hajinasab, Saeed Saber-Samandari, Sara Ahmadi, and Kadhim Alamara, "Preparation and characterization of a biocompatible magnetic scaffold for biomedical engineering," *Materials Chemistry and Physics*, vol. 204, pp. 378–387, 2018.

[43] Aaron C Small and James H Johnston, "Novel hybrid materials of magnetic nanoparticles and cellulose fibers," *Journal of Colloid and Interface Science*, vol. 331, no. 1, pp. 122–126, 2009.

[44] Hyung-Mun Yun, Su-Jin Ahn, Kyung-Ran Park, Mi-Joo Kim, Jung-Ju Kim, Guang-Zhen Jin, Hae-Won Kim, and Eun-Cheol Kim, "Magnetic nanocomposite scaffolds combined with static magnetic field in the stimulation of osteoblastic differentiation and bone formation," *Biomaterials*, vol. 85, pp. 88–98, 2016.

[45] Hadas Skaat, Ofra Ziv-Polat, Abraham Shahar, David Last, Yael Mardor, and Shlomo Margel, "Magnetic scaffolds enriched with bioactive nanoparticles for tissue engineering," *Advanced healthcare materials*, vol. 1, no. 2, pp. 168–171, 2012.

[46] Claire Gervais, Mathieu Thoury, Solenn Réguer, Pierre Gueriau, and Jennifer Mass, "Radiation damages during synchrotron x-ray micro-analyses of prussian blue and zinc white historic paintings: detection, mitigation and integration," *Applied Physics A*, vol. 121, no. 3, pp. 949–955, 2015.

[47] P Sivakumar, R Ramesh, A Ramanand, S Ponnusamy, and C Muthamizhchelvan, "Synthesis and characterization of nickel ferrite magnetic nanoparticles," *Materials Research Bulletin*, vol. 46, no. 12, pp. 2208–2211, 2011.

[48] Vijaya Barge, Pranali Yendhe, Kavita Kodre, Sneha Attarde, and Ravindra Patil, "Electron microscopy: A review," 2014.

[49] Anjali Priya, Abhishek Singh, and Nikhil Anand Srivastava, "Electron microscopy–an overview," *International Journal of Students' Research in Technology & Management*, vol. 5, no. 4, pp. 81–87, 2017.

[50] Fabien Destic and Christophe Bouvet, "Impact damages detection on composite materials by THz imaging," *Case studies in nondestructive testing and evaluation*, vol. 6, pp. 53–62, 2016.

[51] Egor V Yakovlev, Kirill I Zaytsev, Irina N Fokina, Valeriy E Karasik, and Stanislav O Yurchenko, "Nondestructive testing of polymer composite materials using THz radiation," in *Journal of Physics: Conference Series*. IOP Publishing, 2014, vol. 486, p. 012008.

[52] I Amenabar, F Lopez, and A Mendikute, “In introductory review to THz non-destructive testing of composite mater,” *Journal of Infrared, Millimeter, and Terahertz Waves*, vol. 34, no. 2, pp. 152–169, 2013.

[53] Sonia Zappia, Lorenzo Crocco, and Ilaria Catapano, “Thz imaging for food inspections: A technology review and future trends,” 2021.

[54] R Scapaticci, S Zappia, I Catapano, G Ruello, G Bellizzi, N Pasquino, M Cavagnaro, S Pisa, E Piuzzi, F Frezza, et al., “Broadband electromagnetic sensing for food quality control: A preliminary experimental study,” in *2021 15th European Conference on Antennas and Propagation (EuCAP)*. IEEE, 2021, pp. 1–5.

[55] S Zappia, R Scapaticci, , G Ruello, L Crocco, and I Catapano, “Non-destructive inspection of chocolate cream with thz imaging,” *2023 17th European Conference on Antennas and Propagation (EuCAP)*, pp. 1–5, 2023.

[56] Sonia Zappia, Lorenzo Crocco, Rosa Scapaticci, and Ilaria Catapano, “Terahertz inspections of chocolate cream samples,” *proceeding of 2022 XXIV National Meeting of Electromagnetics (Rinem 2022), Catania (Italy).*

[57] S Zappia, I Catapano, R Scapaticci, and Crocco, “Terahertz imaging for food quality inspection,” *proceeding of VI National Conference “Interaction between electromagnetic fields and biosystems (ICEmB 2022), Cagliari (Italy).*

[58] Matteo Bruno Lodi, Nicola Curreli, Sonia Zappia, Luca Pilia, Maria Francesca Casula, Sergio Fiorito, Ilaria Catapano, Francesco Desogus, Teresa Pellegrino, Ilka Kriegel, et al., “Influence of magnetic scaffold loading patterns on their hyperthermic potential against bone tumors,” *IEEE transactions on bio-medical engineering*, 2021.

[59] Sonia Zappia, Rosa Scapaticci, Matteo Bruno Lodi, Alessandro Fanti, Giuseppe Ruello, Lorenzo Crocco, and Ilaria Catapano, “Non-destructive characterization of magnetic polymeric scaffolds using terahertz time-of-flight imaging,” *IEEE Transactions on Terahertz Science and Technology*, 2023.

[60] S Zappia, L Crocco, R Scapaticci, MB Lodi, A Fanti, and I Catapano, “Terahertz imaging of magnetic scaffolds,” *proceeding of VI National Conference “Interaction between electromagnetic fields and biosystems (ICEmB 2022), Cagliari (Italy).*

[61] S Zappia, I Catapano, R Scapaticci, MB Lodi, A Fanti, and L Crocco, “Magnetic nanoparticles distribution estimate in polymeric scaffolds using THz imaging,” *proceeding of 2022 XXIV National Meeting of Electromagnetics (Rinem 2022), Catania (Italy).*

[62] Piotr Garbacz, "Terahertz imaging–principles, techniques, benefits, and limitations," *Problemy Eksploatacji*, , no. 1, pp. 81–92, 2016.

[63] Leili Afsah-Hejri, Parvaneh Hajeb, Parsa Ara, and Reza J Ehsani, "A comprehensive review on food applications of terahertz spectroscopy and imaging," *Comprehensive Reviews in Food Science and Food Safety*, vol. 18, no. 5, pp. 1563–1621, 2019.

[64] Fabian Friederich, Wolff Von Spiegel, Maris Bauer, Fanzhen Meng, Mark D Thomson, Sebastian Boppel, Alvydas Lisauskas, Bernd Hils, Viktor Krozer, Andreas Keil, et al., "Thz active imaging systems with real-time capabilities," *IEEE Transactions on Terahertz Science and Technology*, vol. 1, no. 1, pp. 183–200, 2011.

[65] Gregor Klatt, Raphael Gebs, Hanjo Schäfer, Michael Nagel, Christof Janke, Albrecht Bartels, and Thomas Dekorsy, "High-resolution terahertz spectrometer," *IEEE journal of selected topics in quantum electronics*, vol. 17, no. 1, pp. 159–168, 2010.

[66] Miriam Serena Vitiello and Alessandro Tredicucci, "Tunable emission in thz quantum cascade lasers," *IEEE Transactions on Terahertz Science and Technology*, vol. 1, no. 1, pp. 76–84, 2011.

[67] B Gorshunov, A Volkov, I Spektor, A Prokhorov, A Mukhin, Martin Dressel, S Uchida, and Alois Loidl, "Terahertz bwo-spectrosopy," *International Journal of Infrared and Millimeter Waves*, vol. 26, pp. 1217–1240, 2005.

[68] ER Brown, KA McIntosh, KB Nichols, and CL Dennis, "Photomixing up to 3.8 thz in low-temperature-grown gaas," *Applied Physics Letters*, vol. 66, no. 3, pp. 285–287, 1995.

[69] J Amorim, G Baravian, M Touzeau, and J Jolly, "Two-photon laser induced fluorescence and amplified spontaneous emission atom concentration measurements in o2 and h2 discharges," *Journal of applied physics*, vol. 76, no. 3, pp. 1487–1493, 1994.

[70] Marcel JE Golay, "The theoretical and practical sensitivity of the pneumatic infra-red detector," *Review of Scientific Instruments*, vol. 20, no. 11, pp. 816–820, 1949.

[71] Adrian Dobroiu, Chiko Otani, and Kodo Kawase, "Terahertz-wave sources and imaging applications," *Measurement Science and Technology*, vol. 17, no. 11, pp. R161, 2006.

[72] MenloSystem. [Online]. Available: //www.menlosystems.com/products/thz-time-domain solutions/, ," .

[73] Albrecht Bartels, Roland Cerna, Caroline Kistner, Arne Thoma, Florian Hudert, Christof Janke, and Thomas Dekorsy, “Ultrafast time-domain spectroscopy based on high-speed asynchronous optical sampling,” *Review of Scientific Instruments*, vol. 78, no. 3, pp. 035107, 2007.

[74] Dominik Stehr, Christopher M Morris, Christian Schmidt, and Mark S Sherwin, “High-performance fiber-laser-based terahertz spectrometer,” *Optics letters*, vol. 35, no. 22, pp. 3799–3801, 2010.

[75] DM Mittleman, J Cunningham, MC Nuss, and M Geva, “Noncontact semiconductor wafer characterization with the terahertz hall effect,” *Applied Physics Letters*, vol. 71, no. 1, pp. 16–18, 1997.

[76] Chen Wang, Ruiyun Zhou, Yuxin Huang, Lijuan Xie, and Yibin Ying, “Terahertz spectroscopic imaging with discriminant analysis for detecting foreign materials among sausages,” *Food Control*, vol. 97, pp. 100–104, 2019.

[77] S Wang and XC Zhang, “Pulsed terahertz tomography,” *Journal of Physics D: Applied Physics*, vol. 37, no. 4, pp. R1, 2004.

[78] Jun Takayanagi, Hiroki Jinno, Shingo Ichino, Koji Suizu, Masatsugu Yamashita, Toshihiko Ouchi, Shintaro Kasai, Hideyuki Ohtake, Hirohisa Uchida, Norihiko Nishizawa, et al., “High-resolution time-of-flight terahertz tomography using a femtosecond fiber laser,” *Optics express*, vol. 17, no. 9, pp. 7533–7539, 2009.

[79] Mario Bertero and Patrizia Boccacci, *Introduction to inverse problems in imaging*, CRC press, 1998.

[80] Bradley Ferguson, Shaohong Wang, Doug Gray, Derek Abbot, and X-C Zhang, “T-ray computed tomography,” *Optics Letters*, vol. 27, no. 15, pp. 1312–1314, 2002.

[81] Loren T Niklason, Bradley T Christian, Laura E Niklason, Daniel B Kopans, Donald E Castleberry, BH Opsahl-Ong, Cynthia E Landberg, Priscilla J Slanetz, Angela A Giardino, Richard Moore, et al., “Digital tomosynthesis in breast imaging.,” *Radiology*, vol. 205, no. 2, pp. 399–406, 1997.

[82] Max Born and Emil Wolf, “Principles of optics, chapter 1,” 1999.

[83] Charles F Van Loan, “Generalizing the singular value decomposition,” *SIAM Journal on numerical Analysis*, vol. 13, no. 1, pp. 76–83, 1976.

[84] Gene H Golub and Christian Reinsch, “Singular value decomposition and least squares solutions,” in *Linear Algebra*, pp. 134–151. Springer, 1971.

[85] Harry Andrews and C Patterson, “Singular value decompositions and digital image processing,” *IEEE Transactions on Acoustics, Speech, and Signal Processing*, vol. 24, no. 1, pp. 26–53, 1976.

[86] Jianyuan Qin, Yibin Ying, and Lijuan Xie, “The detection of agricultural products and food using terahertz spectroscopy: a review,” *Applied Spectroscopy Reviews*, vol. 48, no. 6, pp. 439–457, 2013.

[87] Teruo Jyo, Hiroshi Hamada, Daisuke Kitayama, Makoto Yaita, and Hideyuki Nosaka, “An accurate permittivity measurement using interferometric phase noise averaging for terahertz imaging,” *IEEE Transactions on Terahertz Science and Technology*, vol. 8, no. 3, pp. 278–286, 2018.

[88] Brahatheeswaran Dhandayuthapani, Yasuhiko Yoshida, Toru Maekawa, and D Sakthi Kumar, “Polymeric scaffolds in tissue engineering application: a review,” *International journal of polymer science*, vol. 2011, 2011.

[89] Lisa E Freed and Gordana Vunjak-Novakovic, “Culture of organized cell communities,” *Advanced drug delivery reviews*, vol. 33, no. 1-2, pp. 15–30, 1998.

[90] Vassilis Karageorgiou and David Kaplan, “Porosity of 3d biomaterial scaffolds and osteogenesis,” *Biomaterials*, vol. 26, no. 27, pp. 5474–5491, 2005.

Author's Publications

International journal papers

Lodi M. B., Curreli N., **Zappia S.**, Pilia L., Casula M. F., Fiorito S., Catapano I., Desogus F., Pellegrino T., Kriegel I., Crocco L., Mazzarella G., Fanti A. (2021).
Influence of magnetic scaffold loading patterns on their hyperthermic potential against bone tumors.
IEEE Transactions on Biomedical Engineering, 69(6), 2029-2040.
DOI: 10.1109/TBME.2021.3134208

Zappia S., Scapaticci R., Lodi M.B., Fanti A., Ruello G., Crocco L., Catapano I. (2023)
Non-Destructive Characterization of Magnetic Polymeric Scaffolds using Terahertz Time-of-Flight Imaging
IEEE Transactions on Terahertz Science and Technology - (Accepted paper)

International book chapter

Zappia S., Crocco L., Catapano I. (2021)
Book title: Terahertz Technology
Chapter title: THz Imaging for food inspections: A technology review and future trends.
Intechopen, DOI: 10.5772/intechopen.97615

International conference papers

Scapaticci R., **Zappia S.**, Catapano I., Ruello G., Bellizzi G., Pasquino N., Cavagnaro M., Pisa S., Piuzzi E., Frezza F., Vipiana F., Tobon Vasquez J.A., Ricci M., Crocco, L. (2021, March).
Broadband Electromagnetic Sensing for Food Quality Control: A Preliminary Experimental Study.
In 2021 15th European Conference on Antennas and Propagation (EuCAP) .

Online, 15-20/03/2020, (pp. 1-5), IEEE, DOI: 10.23919/EuCAP51087.2021.9411022

Catapano I., **Zappia S.**, Ludeno G., Soldovieri F.
THz Imaging activities at IREA - CNR
9th International THz-Bio Workshop, Online Meeting, Apr. 19-23 2021, in Workshop Co-chairs (p.65), CNR, link: /THz-BioWorkshop-libro-defcompressed.pdf.

Scapaticci R., Palmeri R., Ricci M., Tobon Vasquez J.A., **Zappia S.**, Vipiana F., Crocco L.
Contaminants Detection in Industrial Products Through Microwave Imaging and Compressive Sensing Techniques
Ursi International Symposium on Electromagnetic Theory 2023, (URSI) EMTS 2023
University of British Columbia Vancouver, BC, Canada, 23-26 May 2023 (Accepted Conference Paper)

Zappia S., Scapaticci R., Ruello G., Crocco L., Catapano I.
Non-Destructive Inspection of Chocolate Cream with THz Imaging
In 2023 17th European Conference on Antennas and Propagation (EuCAP).
Florence, Italy, 26-31 March 2023, IEEE (not yet available online)

National conference papers

Zappia S., Catapano I., Scapaticci R., Crocco L.
Terahertz Imaging for Food Quality Inspection
VI National Conference Interaction between electromagnetic fields and biosystems, (ICEmB 2022),
Cagliari (Italy), July 2022

Zappia S., Crocco L., Scapaticci R., Lodi M.B., Fanti A., and Catapano I.
Terahertz imaging of magnetic scaffolds
VI National Conference Interaction between electromagnetic fields and biosystems, (ICEmB 2022),
Cagliari (Italy), July 2022

Zappia S., Crocco L., Scapaticci R., Catapano I.
TeraHertz Inspections of Chocolate Cream Samples
11th URSI ITNC Meeting
Catania (Italy), September 2022

Zappia S., Catapano I., Scapaticci R., Lodi M.B., Fanti A., Crocco L.
Magnetic nanoparticles distribution estimate in polymeric scaffolds using THz

imaging
2022 XXIV National Meeting of Electromagnetics (Rinem 2022), Catania (Italy).